# Measurement of $^{238}\mathrm{U}(n,n'\gamma)$ cross section data and their impact on reaction models

M. Kerveno, M. Dupuis, A. Bacquias, F. Belloni, D. Bernard, C. Borcea, M. Boromiza, R. Capote, C. de Saint Jean, P. Dessagne, et al.

# Measurement of $^{238}$U$(n, n'\gamma)$ cross section data and their impact on reaction models

M. Kerveno,[1,*] M. Dupuis,[2,3] A. Bacquias,[1] F. Belloni,[4] D. Bernard,[5] C. Borcea,[6] M. Boromiza,[6] R. Capote,[7] C. De Saint Jean,[2,3] P. Dessagne,[1] J. C. Drohé,[4] G. Henning,[1] S. Hilaire,[2,3] T. Kawano,[8] P. Leconte,[5] N. Nankov,[4] A. Negret,[6] M. Nyman,[4] A. Olacel,[6] A. J. M. Plompen,[4] P. Romain,[2,3] C. Rouki,[4] G. Rudolf,[1] M. Stanoiu,[6] and R. Wynants[4]

[1]*Université de Strasbourg, CNRS, IPHC/DRS UMR 7178, 23 Rue du Loess, F-67037 Strasbourg, France*

[2]*CEA, DAM, DIF, F-91297 Arpajon, France*

[3]*Université Paris-Saclay, CEA, Laboratoire Matière sous Conditions Extrêmes, 91680 Bruyères-Le-Châtel, France*

[4]*European Commission, Joint Research Centre, Retieseweg 111, B-2440 Geel, Belgium*

[5]*CEA, DES, IRESNE, DER, SPRC, LEPh, F-13108 Saint-Paul-lez-Durance, France*

[6]*Horia Hulubei National Institute for Physics and Nuclear Engineering, 077125 Bucharest-Măgurele, Romania*

[7]*Nuclear Data Section, International Atomic Energy Agency, Wagramer Strasse, A-1400 Vienna, Austria*

[8]*Los Alamos National Laboratory, Los Alamos, New Mexico 87545, USA*

(Received 16 April 2021; accepted 25 August 2021; published xxxxxxxxxx)

A better knowledge of $(n, xn)$ reaction cross sections is important for both reaction modeling and energy applications. This article focuses on inelastic scattering of neutrons off $^{238}$U for which improvements are needed to better constrain evaluations and solve inconsistencies in nuclear power reactor calculations. A new precise measurement of $(n, xn\gamma)$ reaction cross sections on $^{238}$U has been performed at the GELINA (Geel Electron LINear Accelerator) neutron facility operated by EC-JRC-Geel (Belgium) with the GRAPhEME (GeRmanium array for Actinides PrEcise MEasurements) setup. The prompt $\gamma$-ray spectroscopy method coupled to time-of-flight measurements is used to extract $(n, xn\gamma)$ cross section values which can be further combined to infer the total neutron inelastic scattering cross section. Cross section data for 18 $\gamma$ transitions (five never measured before) are presented and compared to the data in the literature. Emphasis is especially given to the uncertainty determination to produce partial cross section data as accurate as possible. Due to intrinsic limitations of the experimental method, the use of additional nuclear structure information coupled with theoretical modeling is required to determine the total $(n, n')$ cross section over the whole neutron energy range. We have investigated modeling aspects of the $^{238}$U$(n, n'\gamma)$ cross sections related to the description of compound nucleus and preequilibirum mechanisms as well as the discrete part of nuclear structure. Through comparison between experimental and calculated $(n, n'\gamma)$ cross sections, we pinpoint inaccuracies in the description of specific reaction mechanisms and challenge recently implemented models. This helps improving the whole modeling of the $(n, n')$ reaction.

DOI: 10.1103/PhysRevC.00.004600

## I. INTRODUCTION

An accurate theoretical description of the various competing mechanisms involved during the collision between a medium energy neutron and a target nucleus remains a challenge. Precise and specific measurements are needed to validate, constrain, and identify the aspects of the modeling that need improvement.

The important reaction discussed in the present study is the collision of a neutron with a $^{238}$U target which is the most abundant nucleus in present day nuclear power reactors. A precise knowledge of the $^{238}$U$(n, n')$ inelastic process, as it strongly contributes to the slowing down of the fast neutrons, is required to optimize new reactor designs [1] and to accurately model current light water reactors (especially their radial power map). These reactor studies are made with neutron transport simulation codes which use evaluation files as inputs. These files contain all the nuclear physics parameters required to describe the interaction between particles with matter. The evaluation process combines information from experimental data and state of the art of theoretical modeling to produce the best estimation of a nuclear observable like cross sections. On top of that, experimental reactor validation studies are performed to provide insights on the integrated cross sections of specific reaction channels [2]. In Ref. [2], the comparison between calculated and experimental values (of multiplication factors and neutron spectral indices for natural uranium reflected critical spheres and parallelograms) showed a clear overestimation by about $(10 \pm 2)$% of the JEFF-3.1.1 $^{238}$U$(n, n')$ inelastic scattering off the continuum in the 2–5 MeV energy region [3]. Finally, it has been shown that to meet the target accuracy of large reactor simulations, the uncertainty for the $(n, n')$ cross section should be about 2% to 3% [1,4]. All these considerations lead thus to the need of a new and accurate measurement of the $^{238}$U$(n, n')$ cross section.

Measuring and modeling $(n, n')$ cross section is challenging leading to large uncertainties. Therefore it features prominently in the High Priority Request List (HPRL)

*maelle.kerveno@iphc.cnrs.fr

 

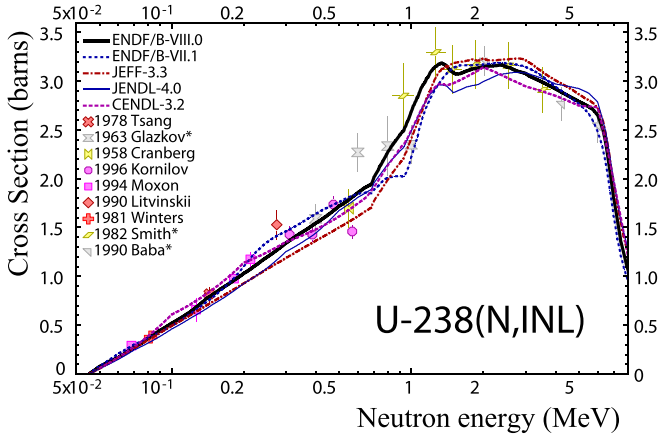


FIG. 1. Evaluated [21–26] and experimental $^{238}$U inelastic scattering cross section data [7,8,10–16]. The experimental data marked with * have been corrected using model calculations.

of the Nuclear Energy Agency (NEA) [4] to encourage the experimental community to produce accurate new measurements.

A large amount of data (total and partial cross section) related to the $^{238}\mathrm{U}(n,n')$ reaction are present in the EXFOR database [5]. The first referenced measurement was published in 1956 and the last one in 2009. All these experiments rely on different techniques (time of flight [6–8], transmission [9], prompt $\gamma$-ray spectroscopy [6], etc.), different detection instruments (proportional counter [10], scintillator [8,11–13], $^{3}$He counter [14], etc.) and several facilities (reactor [10,15], Van de Graaff [7,11,16] or LINAC [6,8,12] accelerators, etc.). Up to 200 keV, the cross section of the first excited level production can be used as total inelastic [12], as the second level contribution is small. And finally, partial data complemented with model calculations to provide total cross section values can be also considered for the 1 to 5 MeV neutron energy range (e.g., [13,17]). Figure 1 compiles $^{238}\mathrm{U}(n,n')$ cross sections from experimental (EXFOR [5]) and evaluated data files. Despite these experimental data sets, large differences are still present between evaluations as also highlighted in the CIELO project [18].

A better knowledge of the $^{238}\mathrm{U}(n,n')$ cross section requires both experimental efforts and model improvements. The modeling-experiment complementarity is especially important for the prompt $\gamma$-ray spectroscopy method [19,20], which allows the measurements of $\gamma$-ray production cross sections $(n,xn\gamma)$ and from which the total $(n,xn)$ cross section can be deduced using level and decay sequence information from literature. Theoretical modeling is needed when experimental information is missing. Another approach would be to calculate $(n,xn)$ cross sections using theoretical models *a priori* constrained or improved by comparisons to the experimental $(n,xn\gamma)$ data [20]. To pinpoint model inaccuracies and thus help improving the whole modeling of the reaction, new advances in the description of compound nucleus reactions and preequilibrium emission as well as variations on the nuclear structure description are tested through a comparison to these new measurements.

In this paper, we present the experimental effort to measure new accurate and reliable $^{238}\mathrm{U}(n,n'\gamma)$ cross section data and new theoretical developments that could be used in the future to produce a more precise total inelastic cross section.

The second section describes the experimental part of the work. The facility and experimental devices used to measure $(n,n'\gamma)$ cross section are presented as well as the data analysis procedure and uncertainty determination. In the third section, the new cross section data are compared to existing ones. In the fourth section, calculations are compared to experimental data. The main modeling aspects of the $(n,n'\gamma)$ reaction are also recalled. Then, specific modeling features related to the compound nucleus and preequilibrium emission processes are discussed. Finally, the fifth section emphasizes the importance of the $^{238}$U nuclear structure knowledge for such studies through a sensitivity study based on Monte Carlo (MC) calculations, and variations of the discrete levels description. A conclusion ends the paper and an outlook is given.

## II. THE GRAPHEME SETUP AT GELINA AND DATA ANALYSIS

This section is devoted to the description of the experimental setup and data analysis procedure used for these measurements. As detailed descriptions have been made already in previous publications [27,28], emphasis will be given here only on specific items related to the $^{238}\mathrm{U}(n,xn\gamma)$ measurements.

### A. The GELINA neutron beam facility and the GRAPhEME setup

The reported measurement was performed with the GRAPhEME setup [28] at the GELINA neutron beam facility operated by EC-JRC-Geel (Belgium) [29,30]. The neutrons are produced by photofission and $(\gamma,xn)$ reactions in a depleted uranium target [31]. They are emitted with a characteristic mix of a fission (20%) and an evaporation spectrum (neutron energies from a few eV to 20 MeV). They fly along 12 flight paths around the production source. A moderator is placed above and below the target to extend the neutrons' spectrum down to several meV. However, the GRAPhEME spectrometer, placed at 30 m from the neutron source, is not viewing the moderators, but views directly the uranium target. GRAPhEME is composed of four high purity germanium (HPGe) planar detectors for $\gamma$ detection and a fission chamber for the neutron flux determination. The signals (time and energy) from the detectors are recorded by a digital acquisition system based on TNT2 cards [32] (14 bits for amplitude resolution and a 100 MHz sampling frequency). Figure 2 presents a part of the two-dimensional ($\gamma$-ray energy versus time of flight) distribution obtained for one detector during the $^{238}$U measurement campaign.

The germanium detectors, named G110, B110, G150 and R150, are placed around the sample at 110° and 150° with regards to the neutron beam to allow the precise angular integration of the $\gamma$-ray production cross sections. The design of GRAPhEME has been optimized for measurements with actinide samples. The efficiency of each HPGe detector has

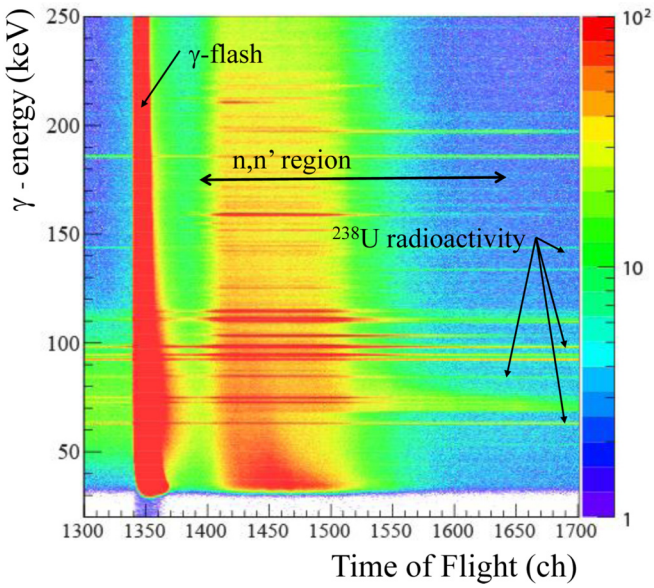


FIG. 2. Two-dimensional plot for $\gamma$-ray energy (keV) as a function of the time of flight (channels) where one sees the $\gamma$ rays from different sources [$\gamma$ flash, $^{238}$U radioactivity, $(n, xn)$ reactions, etc.].

been precisely studied with source measurements ($^{152}$Eu) coupled with MCNPX simulations [33]. To take into account the spatial distribution of the neutron beam (55 mm in diameter), source measurements have been performed with point sources at different positions relative to the center of the beam and also with an extended source. If the sample is radioactive, the radioactive decay can also be used for efficiency calibration. Once the detectors geometry is well defined, the production for each $\gamma$ transition is simulated including the $^{238}$U sample to take into account the self-absorption of the $\gamma$'s in the sample. For the fission chamber, as described in Ref. [27], its operation has been optimized to maximize the efficiency of detection.

### B. $^{238}$U sample

A good knowledge of the sample details is crucial for an accurate determination of the cross sections. Indeed, the number of $^{238}$U atoms appears directly in the cross section formula but, in addition, the composition and the size of the sample play an important role in the $\gamma$-ray efficiency calculation (via the $\gamma$-ray attenuation coefficient) [27]. To obtain an accurate estimation of the number of $^{238}$U atoms contained in the $^{nat}$U sample, and beyond the information given by the manufacturer (Goodfellow), we take advantage of the radioactive nature of the sample, as follows. From the manufacturer we obtained a $^{nat}$U sample which is a rolled sample (disk) made of 99.9% natural uranium with a diameter and thickness of respectively 70.0(5) mm and 0.18(4) mm, according to the specifications of Goodfellow. The huge uncertainty on the thickness (20%) is far from satisfactory, thus the sample was characterized by the target laboratory of EC-JRC-Geel (Belgium). The measurements give a mass of 10.61911(7) g and diameter and thickness of 70.16(3) mm and 0.181(6) mm, respectively. The given uncertainties of the thickness and a diameter are the standard deviations of several measurements. These numbers lead to an apparent density of 15.173 g/cm$^3$ which does not correspond to the one of pure metallic uranium (18.95 g/cm$^3$ [34]). To determine the real mass of $^{238}$U, we measured with GRAPhEME the $\gamma$-ray energy distribution from the radioactivity of the sample. To estimate, using MCNPX simulations, the efficiency of the HPGe detectors for these $\gamma$ lines we introduce oxidation to take into account the apparent density. As already done in the work mentioned in Ref. [27], the sample is considered to have a core of natural uranium (density 18.95 g/cm$^3$) surrounded by layers of $UO_2$ (density 10.97 g/cm$^3$); the thicknesses of the different regions are deduced using the apparent density. The determination of the $^{238}$U mass was made using the 1001.03 keV $\gamma$ line from $^{238}$U radioactivity registered in the four HPGe detectors. The result is the average of nine measurements which leads to a mass of $^{238}$U equal to 10.54(23) g.

### C. Data analysis

More then 3000 hours of beam time have been collected during different campaigns over three years. During such long time measurement, instabilities in the electronics or problems with detectors are not rare and the first step of the analysis is thus the meticulous check of each run, for energy and time channels of each detector, to choose only very stable ones. This allows the summation of statistics for all selected runs without degrading the time and/or energy resolutions. The result of this selection is a collecting time of 2139 h for two HPGe detectors and 731 h and 1139 h for the two others. Once the data sets are prepared, we proceed to the $\gamma$-lines identification. The very good resolutions of the germanium detectors (0.7 keV at 122 keV) and time-of-flight measurement allow a precise selection of $\gamma$ rays from $(n, n')$, $(n, 2n)$, and $(n, 3n)$ processes and their discrimination in respect to other background $\gamma$ lines (radioactivity, fission products, shielding materials). Figure 3 shows portions of the $\gamma$-ray energy distribution for one detector from 20 to 950 keV and for the same time windows width in the radioactivity and inelastic scattering region. Peaks from the $^{238}$U$(n, n')$ reaction are highlighted. To describe the excitation function, $\gamma$ spectra are generated from the bidimensional matrix for appropriate time (neutron energy) binning. The number of counts in each $\gamma$ peak of interest is then determined for each time window. Here a careful analysis has been done for all contaminated peaks by $\gamma$ rays coming from radioactivity, fission products, or other reaction processes which occurred in surrounding materials. As explained in Ref. [28], the GF3 software [35] is used to extract the appropriate number of $\gamma$'s with the following procedure. A first fit of the peak (and its surroundings) is performed for a time window corresponding to the entire energy range of the process of interest [$(n, n')$, $(n, 2n)$, or $(n, 3n)$]. This first adjustment allows the determination of the fit parameters with good statistics. Then the adjustment is repeated for each neutron energy window and the number of counts in the peak of interest is determined. For the neutron flux calculation, the same time windows are applied on the the fission chamber bi-dimensional matrix and the number of fission events is deduced. Finally, for every $\gamma$ transition, the

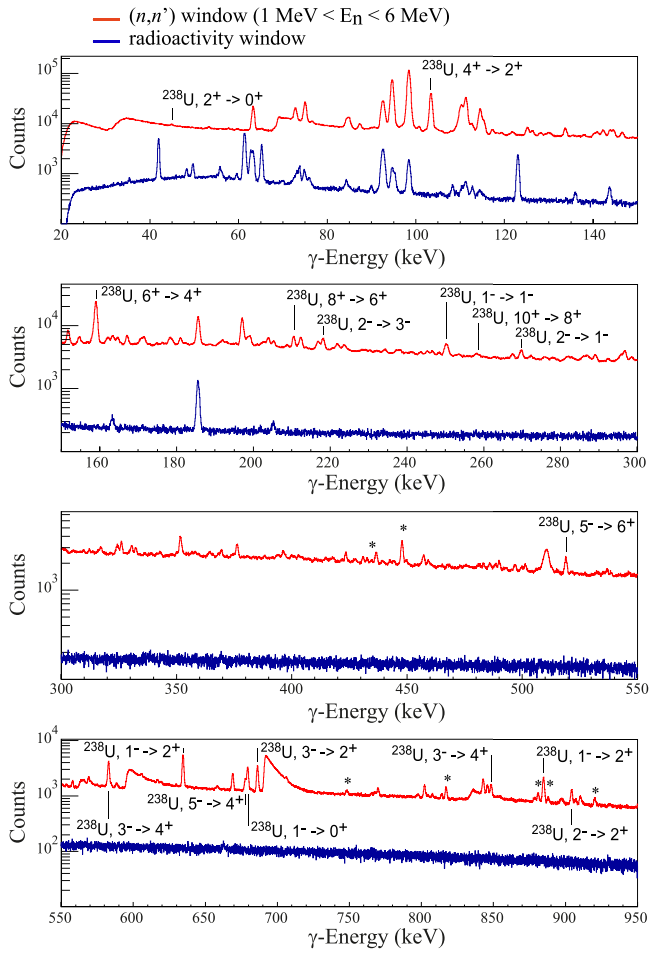


FIG. 3. Portion of $\gamma$-ray energy distributions for one detector from 20 to 950 keV. The red spectra were obtained by applying a time window corresponding to the inelastic scattering incident energies range. The blue spectra correspond to the radioactive decay selected for the same time window width as the red spectra and before the arrival of the neutrons. The $^{238}$U $\gamma$ transitions for which the cross section data are presented in this article are labeled; the others (measured but not shown in this article) are marked with a star.

differential cross section data for each detector (at $\theta_i$ equal to 110° or 150°) and for each neutron energy ($E_n$) are calculated following the formula

$$\frac{d\sigma}{d\Omega}(\theta_i, E_n) = \frac{1}{4\pi}\frac{N_{\rm GE}(\theta_i, E_n)}{N_{\rm FC}(E_n)}\frac{\varepsilon_{\rm FC}}{\varepsilon_{\rm GE}}\frac{\varsigma_{\rm FC}}{\varsigma_{\rm sple}}\frac{1}{\eta_{\rm air}}\sigma_F(E_n), \qquad (1)$$

where $N_{\rm GE}$ and $N_{\rm FC}$ represent the dead time-corrected numbers of counts corresponding to a given $\gamma$ ray in the HPGe detector $i$ and to the fission chamber above the discrimination threshold, respectively, $\varepsilon_{\rm GE}$ and $\varepsilon_{\rm FC}$ are the germanium detector's and the fission chamber's efficiencies, $\sigma_F$ is the $^{235}$U fission cross section [36], $\varsigma_{\rm FC}$ and $\varsigma_{\rm sple}$ are the areal density (atoms/cm$^2$) of target nuclei in the $^{235}$U deposit and in the sample, and $\eta_{\rm air}$ is a correction factor which takes into account the attenuation of neutron beam between the fission chamber and the $^{238}$U sample. In the sample, additional neutrons can

TABLE I. Values and uncertainties of the parameters used in the cross section formula, Eq. (1).

| Parameter | Values | Uncertainty (%) |
|---|---|---|
| $N_{\rm GE}$ ($E_n$) | 100–7000 | 80–1.5 |
| $N_{\rm FC}$ ($E_n$) | $10^4$–$10^5$ | ≃1 |
| $\varepsilon_{\rm FC}$ | 0.94 | 2.1 |
| $\varepsilon_{\rm GE}$ ($E_\gamma$) | $3\times10^{-3}$–$1\times10^{-4}$ | 3 |
| $\varsigma_{\rm sple}$ | $6.897\times10^{20}$ at. cm$^{-2}$ | 2.4 |
| $\varsigma_{\rm FC}$ | $8.3\times10^{17}$ at. cm$^{-2}$ | 0.55 |
| $\sigma_F$ ($E_n$) | 1–2 b | 1.3–1.5 |
| $\eta_{\rm air}$ | 0.98 | 1 |

be produced by fission reactions on $^{238}$U, but also multiple elastic and inelastic scatterings can occur. The resulting neutrons are able to produce $(n, n'\gamma)$ reactions which will be then registered with a bad neutron energy. We have estimated these contributions by calculating the proportion of the secondary neutrons over the incident neutrons in the beam as a function of energy. As the sample is rather thin, this proportion is small: for fission, it is less than 1% up to 8 MeV and reaches only 2% at 11 MeV. The contribution of secondary neutron from elastic and inelastic scatterings is less than 0.3%. Taking into account these numbers, no corrections were applied for these effects. It has to be noticed that for some other data present in EXFOR, this effect was taken into account by added a correction in the cross section calculation.

The angle-integrated $(n, n'\gamma)$ cross section, $\sigma_\gamma$, is obtained by the combination of the differential cross sections through the Gaussian quadrature [37] [Eq. (2)]. Indeed, as detailed in Refs. [27,28], the specific choice of the two angles 110° or 150° allows the exact integration of the $\gamma$-ray angular distribution for transitions with multipolarity up to 3 using Eq. (2),

$$\sigma_\gamma = 2\pi\left[w_1\frac{d\sigma}{d\Omega}(\theta_1) + w_2\frac{d\sigma}{d\Omega}(\theta_2)\right] \qquad (2)$$

where $w_1 = 0.69571$ and $w_2 = 1.30429$ are the weights associated with the angles 150° and 110° respectively. It should be noticed that the cross sections correspond to $\gamma$ production only and are not corrected for internal conversion.

### D. Uncertainties

We have paid particular attention to the estimation of systematic uncertainties associated with the quantities involved in the cross section formula, Eq. (1). In Ref. [19], details are given on their determination. In Table I, we summarize the magnitude (with the range of the parameter value) of the total (systematic and statistical) uncertainties in the case of the $^{238}$U measurement. $N_{\rm GE}$ and $N_{\rm FC}$ are the numbers of counts ($\gamma$'s and fission products) corrected for dead time count loss. For the germanium detectors of GRAPhEME with the data-acquisition specified above, the dead time correction factor varies from 1.2 to 1.6 with a relative uncertainty of 1%. For the fission chamber this factor is 1.003 with a relative uncertainty of 0.01%. One notices in some cases the uncertainty is as high as 80%. This happened at very high incident energies

TABLE II. Selection of identified $\gamma$ energies [38] in the $^{238}$U energy spectra stemming from the $^{238}$U$(n, n')$ reactions. The possible contamination of the peak in the spectra is mentioned in the three last columns. Levels are labeled as $J_k^\Pi$ where $J$ is the level total angular momentum, $\Pi = +/-$ its parity, and $k$ counts the levels of the same $J^\Pi$ by increasing excitation energy.

| | Initial state | | Final state | | | | Peak pollution | | |
|---|---|---|---|---|---|---|---|---|---|
| $E_\gamma$ (keV) | $E$ (keV) | $J_k^\Pi$ | $E$ (keV) | $J_k^\Pi$ | $I_\gamma$ | $\gamma$ multipolarity | Process | $E_\gamma$ (keV) | $E_{\text{level}}$ (keV) |
| 44.915 (13) | 44.916 (13) | $2_1^+$ | 0 | $0_1^+$ | 100 | $E2$ | | | |
| 103.50 (4) | 148.38 (3) | $4_1^+$ | 44.916 (13) | $2_1^+$ | 100 | $E2$ | X $K\beta 3$ | 104.6 | |
| | | | | | | | $^{238}$U$(n, 2n)\,^{237}$U | 103.68 | 159.962 |
| 159.018 (16) | 307.18 (8) | $6_1^+$ | 148.38 (3) | $4_1^+$ | 100 | $E2$ | $^{63}$Cu$(n, \gamma)\,^{64}$Cu | 159.28 | 159.28 |
| 210.6 (4) | 518.1 (3) | $8_1^+$ | 307.18 (8) | $6_1^+$ | 100 | $E2$ | | | |
| 218.1 (3) | 950.12 (20) | $2_1^-$ | 731.93 (3) | $3_1^-$ | 53 (6) | ? | | | |
| 251.2 (7) | 930.55 (9) | $1_2^-$ | 680.11 (4) | $1_1^-$ | 13.1 (14) | ? | $^{238}$U$(n, \gamma)\,^{239}$U | 250.06 | 292.6 |
| 257.8 (4) | 775.9 (4) | $10_1^+$ | 518.1 (3) | $8_1^+$ | 100 | $E2$ | | | |
| 270.1 (4) | 950.12 (20) | $2_1^-$ | 680.11 (4) | $1_1^-$ | 48 (8) | ? | | | |
| 519.46 (8) | 826.64 (11) | $5_1^-$ | 307.18 (8) | $6_1^+$ | 50 (3) | $E1$ | | | |
| 583.55 (3) | 731.93 (3) | $3_1^-$ | 148.38 (3) | $4_1^+$ | 81.4 (16) | $E1$ | $^{208}$Pb$(n, n')\,^{208}$Pb | 583.19 | 3500 |
| | | | | | | | $^{63}$Cu$(n, n')\,^{63}$Cu | 584.82 | 1547 |
| 635.3 (3) | 680.11 (4) | $1_1^-$ | 44.916 (13) | $2_1^+$ | 100.0 (20) | $E1$ | | | |
| 678.3 (3) | 826.64 (11) | $5_1^-$ | 148.38 (3) | $4_1^+$ | 100 (6) | $E1$ | | | |
| 680.2 (5) | 680.11 (4) | $1_1^-$ | 0 | $0_1^+$ | 79 (4) | $E1$ | | | |
| 686.99 (3) | 731.93 (3) | $3_1^-$ | 44.916 (13) | $2_1^+$ | 100 (2) | $E1$ | | | |
| 849.1 (4) | 997.58 (7) | $3_2^-$ | 148.38 (3) | $4_1^+$ | 100 (3) | $E1$ | $^{238}$U$(n, 2n)\,^{237}$U | 849.45 (13) | 905.73 (7) |
| 885.46 (10) | 930.55 (9) | $1_2^-$ | 44.916 (13) | $2_1^+$ | 100 (4) | $E1$ | | | |
| 905.5 (5) | 950.12 (20) | $2_1^-$ | 44.916 (13) | $2_1^+$ | 100 (6) | $E1$ | | | |
| 952.65 (7) | 997.58 (7) | $3_2^-$ | 44.916 (13) | $2_1^+$ | 56.8 (13) | $E1$ | | | |

where both the cross section and the neutron flux are very small and, additionally, in those instances when we had to perform a decomposition of a $\gamma$ line of interest in several contributions. The most common uncertainty values range, however, between 1.5% and 20%.

## III. RESULTS

In the $\gamma$ spectrum, numerous $\gamma$ rays come from inelastic scattering on $^{238}$U. Among these $\gamma$ rays, we were able to determine cross section data for about 40, but not all will be reported here (see Table II). Only a selection of 18 transitions is presented to focus also on the comparison with model calculations. These cross section data are compiled in the EXFOR database [5] as entry number 22795.

Figure 4 shows examples of differential cross section data obtained for the 635-keV $\gamma$ ray coming from the level at 680 keV. From the yield of each detector at 150° and 110°, we can deduce the differential cross section data for each detector at a given angle and these cross sections can then be averaged over the two detectors at that angle $[\frac{d\sigma}{d\Omega}(\theta_i)]$. Finally Eq. (1) is used to obtain the angle-integrated cross section for the given $\gamma$ ray. This quantity is calculated for each pair of detectors and for the four detectors using the Gauss quadrature. This procedure is applied for all transitions and allows verifying that the results of the two detectors at one angle are consistent.

The measured cross sections are compared to four previous measurements performed in 1976 by Voss *et al.* [39], in 1979 by Olsen *et al.* [40], in 2004 by Fotiades *et al.* [6], and in 2009 by Hutcheson *et al.* [41]. Some details on these experiments are summarized in Table III.

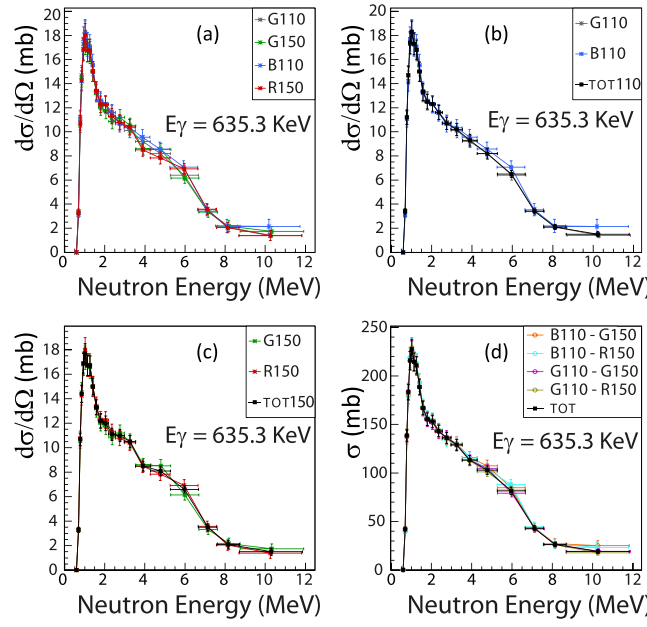


FIG. 4. (a) Differential cross section data at 110° and 150° for each detector (G110, G150, B110, and R150). (b) Differential cross section data at 110° (TOT 110) after adding the statistics for two detectors; (c) the same for 150°. (d) Angle-integrated $(n, n'\gamma)$ cross section data obtained for all the possible combinations of two detectors, "TOT" is the combination of the four detectors.

TABLE III. Summary of the main characteristics of $(n, n'\gamma)$ cross section measurements from the literature (EXFOR).

| Author (year) | Facility | Detector ($\gamma$) | Neutron energy range (MeV) | $\gamma$-ray energy range (keV) | Number of analyzed $\gamma$ transitions |
|---|---|---|---|---|---|
| Voss *et al.* (1976) | Isochronous cyclotron, Karlsruhe Institute of Technology (KIT) (Germany) | Ge(Li) | $\leqslant$5.5 | 584–1061 | 6 |
| Olsen *et al.* (1979) | Oak Ridge electron linear accelerator white neutron source. Oak Ridge National Laboratory (USA) | Ge(Li) | $\leqslant$5 | 448.6–1223.9 | 28 |
| Fotiades *et al.* (2004) | Weapons Neutron Research (WNR) at LANSCE, LANL (USA) | GEANIE detectors (HPGe) | $\leqslant$84 | 103.5–1485 | 24 |
| Hutcheson *et al.* (2009) | Tandem Van de Graaff, Triangle Universities Nuclear Laboratory (USA) | clover and planar HPGe | 5, 6, 10, 12, 14 | 158.8–1060.3 | 7 |

### A. The special case of low energy $\gamma$ rays

As described in detail in reference [19], $\gamma$-ray production cross section data can be used to infer the total $(n, n')$ cross section which is the sum of all the partial cross sections of $\gamma$ rays that feed the ground state (GS). If a transition to the GS from an excited level is not detected for various experimental reasons but another one from the same level is observed, then the cross section for the unobserved transition can be deduced using the branching ratio (if known). This allows us to estimate the $\gamma$-ray production cross section data also for transitions we were not able to detect and, consequently, in particular to construct the total inelastic cross section. In the case of even-even nuclei, the presence of a rotational band built on the GS favors the deexcitation path through this band. The first excited level collects thus a huge part of the $\gamma$ strength and its deexcitation to the GS represents more than 90% of the total cross section in the case of $^{238}$U. A good experimental determination of the $(n, n'\gamma)$ cross section for the deexcitation of the first level is thus of prime importance. The first level in $^{238}$U is only at 44.916 (13) keV and its deexcitation proceeds mainly by internal conversion (internal conversion coefficient = 610 (9) from BRICC v2.3S [42]). As shown in Fig. 3 and despite a long measurement time, the peak corresponding to the 44.9-keV $\gamma$ ray is very weak and placed on a huge background. Only low statistics is achievable for this transition. We note that in this experiment, as $\gamma$ energies range from a few dozen of keV to more than 1 MeV, the $\gamma$ energy range has to be as high as possible. Thus for the low $\gamma$ energies, the data suffer from a well-known "walk" effect of the constant fraction discriminator (CFD): the signal produced by low energy $\gamma$ rays is very weak (near the level of noise) and the CFD digital algorithm can encounter difficulties when extracting the time information. The result in our case is shown in detail in Fig. 5 where the low $\gamma$-ray energy part in the time-amplitude matrix is highlighted. One sees clearly the shift of the $\gamma$ flash to later time (lower neutron energies) resulting in incorrect time assignment for events with energies below around 200 keV.

To correct this effect the following procedure was applied: dedicated beam time was used with a fast timing amplifier between the preamplifier and the TNT cards. In this way, the amplification of the output signal of the preamplifier was

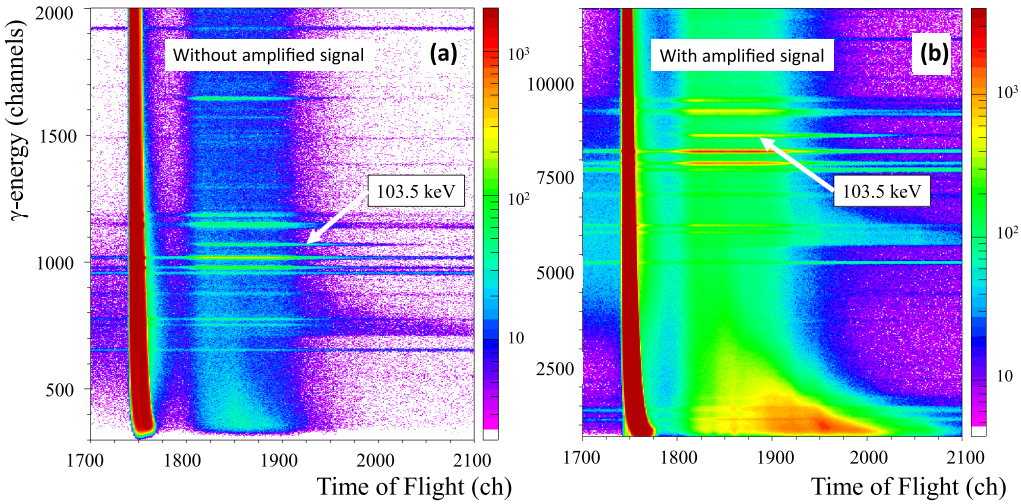


FIG. 5. Zoomed-in look of the time-amplitude matrix corresponding to the low-energy $\gamma$ lines with unamplified (a) and amplified (b) signals. The so-called "walk" effect is clearly visible in panel (a).

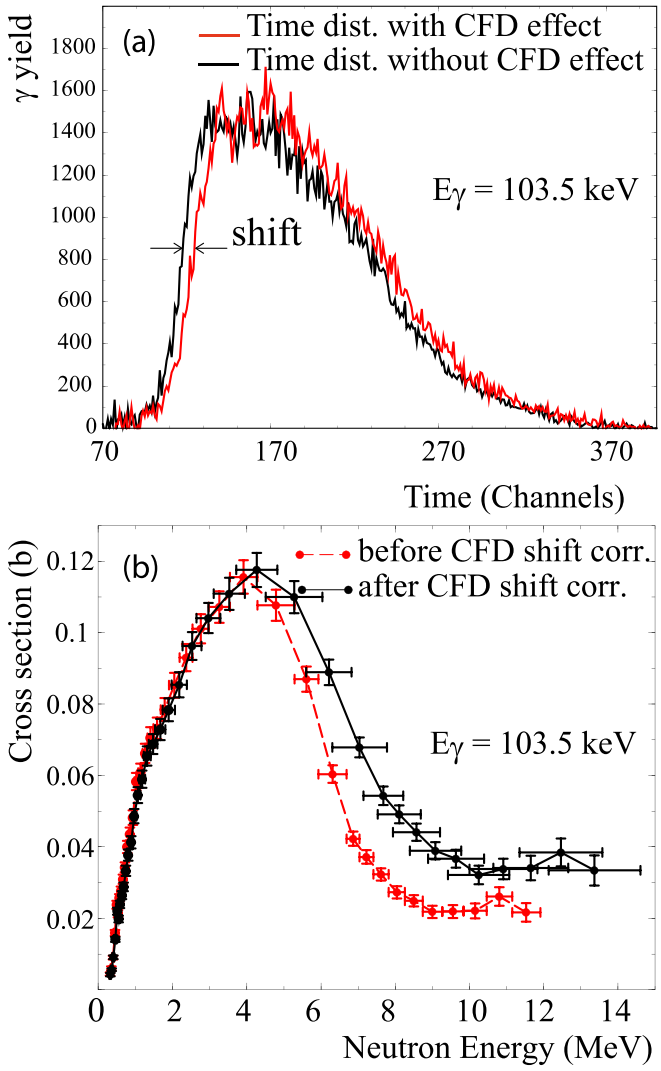


FIG. 6. (a) Time distributions for the detector G110 and for $\gamma$ energy at 103.5 keV. The black distribution is not affected by CFD shift while the red one is. These two distributions are used to define the time correction to apply to the data for each impacted $\gamma$ transition. (b) Cross section data for the 103.5-keV $\gamma$ transition before the CFD shift correction (in red) and after (in black).

increased (the energy range was thus reduced) to shift the low $\gamma$-energy transitions beyond the shift induced by the CFD. The time distributions, for the two settings [see Fig. 6 (top) in the case of the 103.5-keV $\gamma$ line and G110 detector] and for the four detectors, are compared and the time correction is estimated.

This time correction is then used to adjust the data as illustrated in Fig. 6 (bottom) for the 103.5-keV $\gamma$ ray. One sees the high impact on the high neutron energy zone. The uncertainty induced by the correction is taken into account in the uncertainty on the neutron energy bins, which explains the overlap of the errors bars. Three $\gamma$ lines have been corrected for the CFD effect: 44.9, 103.5, and 159.0 keV.

### B. $(n, n'\gamma)$ cross section data

Figures 7 and 8 show all the $\gamma$-production inelastic data on $^{238}$U reported in the present work, with five newly reported cross section data, compared to previous experiments and theoretical calculations. In general, our data are in good agreement with the measurements of Hutcheson *et al.* and systematically higher than the data from Voss *et al.* except for the $\gamma$ ray of 952.7 keV. The comparison with the data of Olsen *et al.* shows that for, in most cases, our cross section data display higher values. This is not the case for the $\gamma$ ray at 680.2 keV because the Olsen datum is the sum of the 678.3- and 680.2-keV transitions. Nine cross section distributions can be compared with the data from Fotiades *et al.*. The data match very well in shape and in magnitude except for the $\gamma$ ray of 952.7 keV (our data are lower) and for the two transitions from the level at 680.2 keV (our data are slightly higher). One can also notice a difference for the 103.5-keV $\gamma$ ray. In this case, the shape and the absolute values of the data are comparable but Fotiades *et al.* data are shifted about 1 MeV towards higher neutron energies (this, however, it is not the case for the other transitions). After several checks (reaction threshold, time distribution, "walk" effect correction; see Sec. III A) no explanation could be found for this difference. It should be mentioned that for the 103.5-keV $\gamma$ ray, the contribution of the 103.7-keV transition from $^{237}$U has not been removed. A first attempt to take this contribution into account was made but the part of the subtracted peak was too high compared to the expected one. This estimation was performed starting from the observed cross section data for the 148.6-keV $\gamma$ ray from the level at 160.0 keV from which the 103.7-keV $\gamma$ ray is also produced. Consequently, we left the 103.5-keV cross section data uncorrected for this $(n, 2n\gamma)$ contribution.

In general, it is difficult to propose explanations of the observed differences between the different data sets as the causes can be multiple (issues with normalization, contamination, correction factor, etc.). In the case of Voss *et al.*, we could suppose an issue with the normalization as the disagreement is the same for all transitions (except for the 952.7-keV $\gamma$ ray). Interestingly, such an underestimation is also present when comparing $(n, n'\gamma)$ cross section data obtained at GELINA [43,44] and those measured by Voss *et al.* [45] for $^{58,60}$Ni and $^{57}$Cr. A way to check the validity of the data is to observe the shape of the cross sections for $\gamma$'s coming from the same excited level. For example, for the level at 731.9 keV, the cross section values of the two $\gamma$'s obtained in this work have the same shape while this is not the case for Olsen *et al.*, which suggests an inconsistency. We can also notice that the 952.7- and 849.1-keV $\gamma$ rays obtained in our work can be questioned. Indeed the peak to plateau ratio at 4 MeV is not the same for the two transitions coming from the same level. Moreover the ratio between the two cross section values, which should be more or less constant, presents some structures at low neutron energy as shown in Fig. 12. This suggests a threshold effect or a contamination which has not been taken into account. The 952.7-keV $\gamma$ ray is in agreement with the previous measurements except with Fotiades *et al.* for neutron energy above 2 MeV. No previous data existfor the 849.1-keV

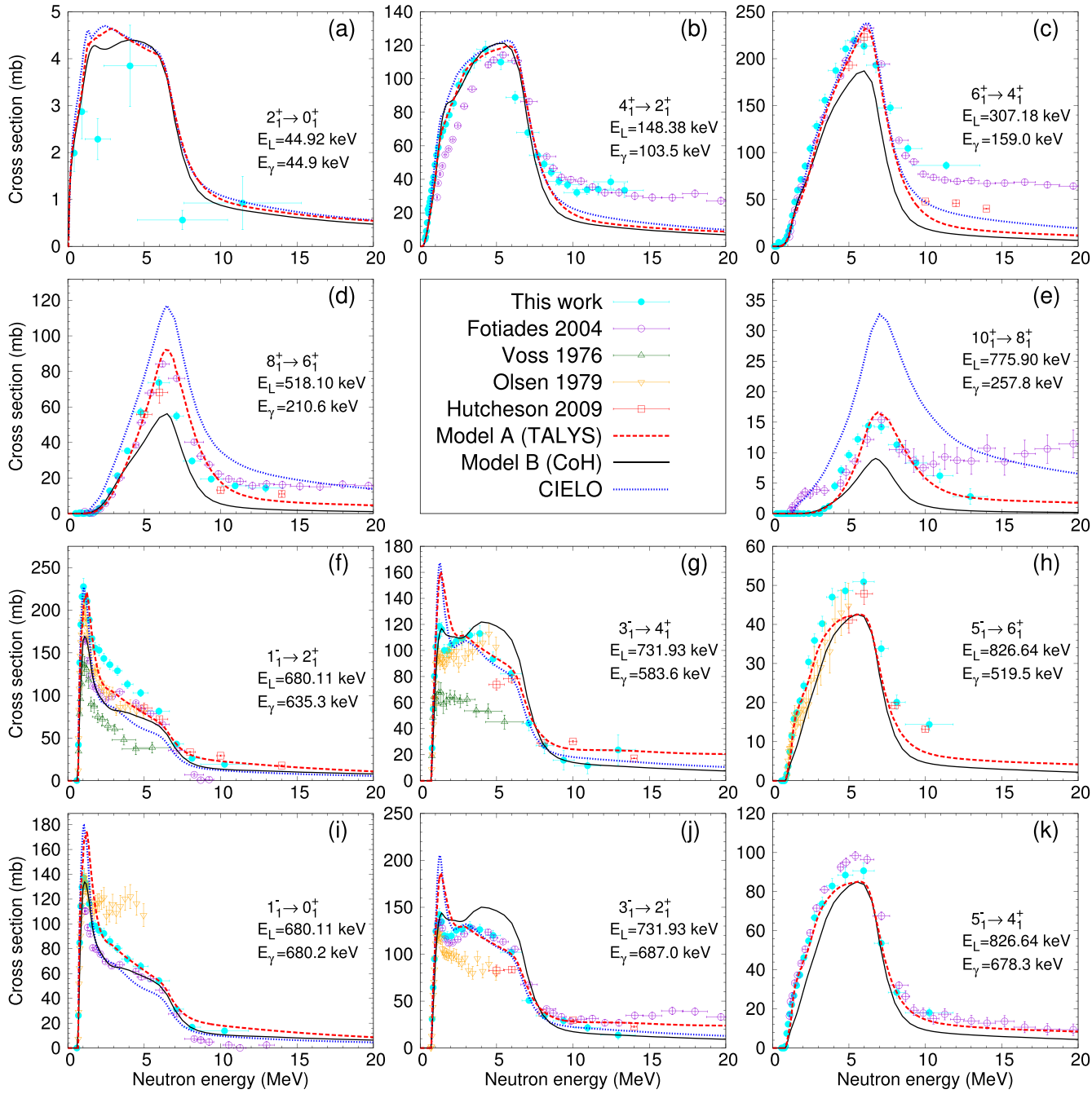


FIG. 7. Experimental $^{238}$U$(n, n'\gamma)$ cross sections (symbols) for $E2$ transitions in the GS band [panels (a)–(e)] or from the levels of the first $K^\Pi = 0^-$ octupole-vibration band to the GS band [panels (f)–(k)], compared to calculations (curves; see details in Sec. IV). The Olsen datum at 680.2 keV corresponds to the sum of the 680.2-keV ($1_1^- \rightarrow 0_1^+$) and 678.3-keV ($5_1^- \rightarrow 4_1^+$) transitions.

transition, so we cannot give a conclusion about the validity of this cross section regarding other data. Despite investigations, as of today, no satisfactory explanation can be given for the questionable shape of the excitation functions of the 849.1- and 952.7-keV $\gamma$ rays. The same situation is encountered for the three $\gamma$ transitions from the level at 950.12 keV (the ratio of peak over plateau is different for the 905-keV $\gamma$ ray compared to the two others).

## IV. MODELING $(n, n'\gamma)$ REACTIONS

### A. Experiments versus calculations

We compare in Figs. 7 and 8 the $(n, n'\gamma)$ cross section values measured by GRAPhEME and the ones from previous experiments with the results of three calculations that represent state of the art for modeling of the $n + ^{238}$U reaction:

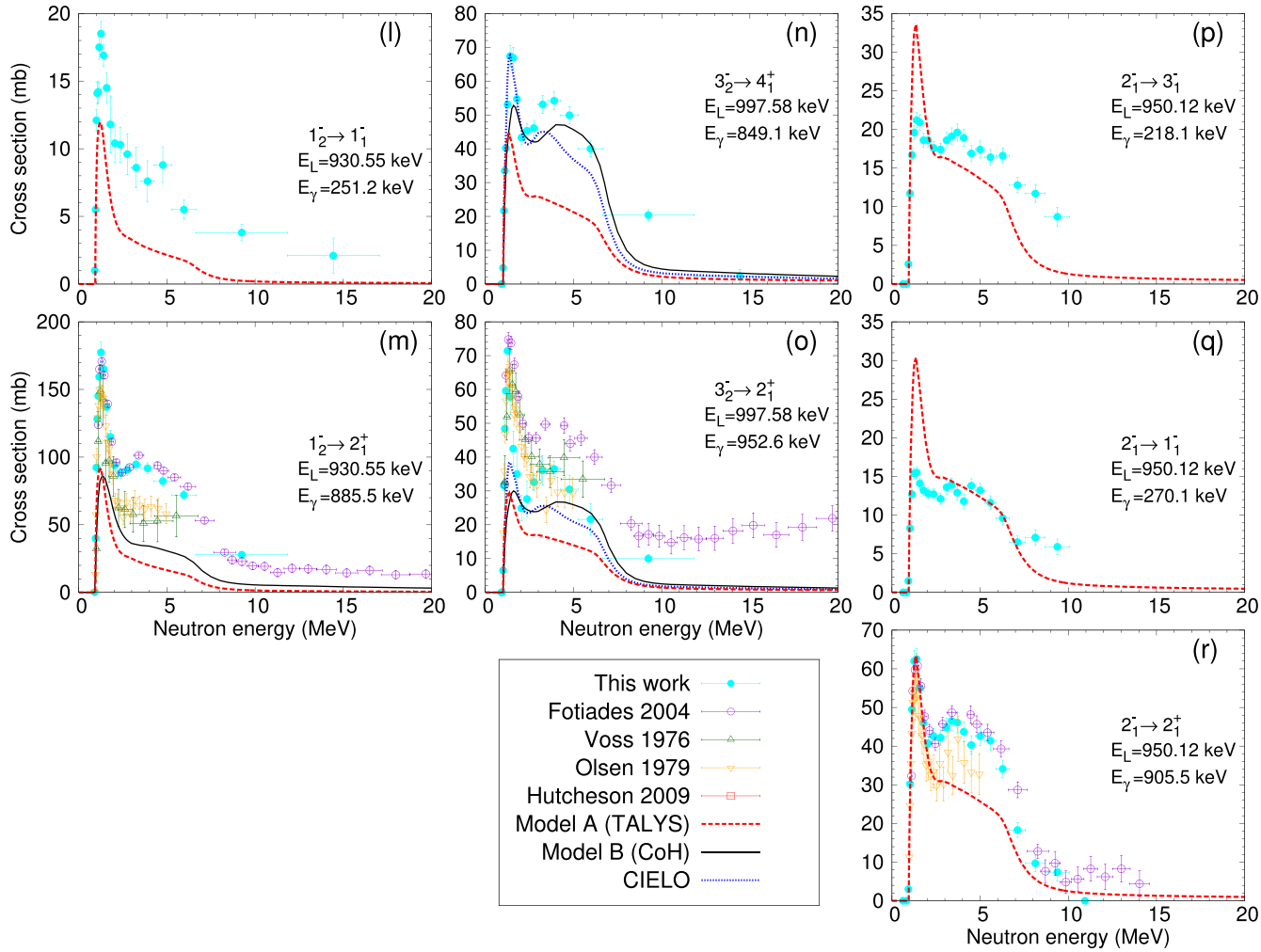


FIG. 8. Same as Fig. 7 for transitions from levels in the $K^\Pi = 1^-, \alpha = 0$ band [46] [panels (p)–(r)] and in the $K^\Pi = 1^-, \alpha = 1$ band [46] [panels (l)–(o)] bands.

(i) Model A is a calculation performed with the TALYS 1.95 code, with almost the same parameters as in Romain *et al.* [47] and a microscopic pre-equilibrium model.
(ii) Model B is a calculation performed with the CoH code [48–50].
(iii) CIELO is the evaluated file adopted by the ENDF/B-VIII.0 library [24]. Calculations [51] have been performed with the EMPIRE code [52].

While the main features of most measured cross sections are fairly well reproduced by the calculations, differences between the three modeling approaches and between models and the measurements are observed. A full understanding of those discrepancies is crucial to clarify which is the best choice of models, parameters, and prescriptions to describe $(n, n'\gamma)$ reactions.

### B. Components of reaction mechanisms

Neutron inelastic scattering leads to the excitation of the target nucleus, which may decay by emitting several $\gamma$ rays. When looking at a specific discrete $\gamma$ line, the production cross section of the $\gamma$ ray $\sigma(\gamma_{i\rightarrow j})$ (electromagnetic transition from the $i$th level to the $j$th level) consists of three components: an $i$th level production cross section $\sigma_i$, a probability to decay to the $j$th level, and a probability of $\gamma$-ray emission instead of internal conversion. This is written as

$$\sigma(\gamma_{i\rightarrow j}) = \sigma_i b(i \rightarrow j)\frac{1}{1+\alpha}, \quad (3)$$

where $\alpha$ is the internal conversion coefficient and $b(i \rightarrow j)$ is the branching bratio (BR).

The $i$th level is populated in several ways. A simple binary reaction ($n + {}^{238}\mathrm{U} \rightarrow {}^{238}\mathrm{U}^* + n'$) leaves the residual nucleus at the $i$th level. This reaction may consist of two reaction mechanisms: the compound inelastic scattering $\sigma_i^{\mathrm{CN}}$ and the direct inelastic scattering $\sigma_i^{\mathrm{DI}}$. The sum $\sigma_i^{\mathrm{CN}} + \sigma_i^{\mathrm{DI}}$ is the actual inelastic scattering cross section of the $i$th level (in previous $\gamma$-ray production studies, this type of level population is often called "side feeding"). When discrete levels or a continuum state higher than the $i$th level can be excited by these mechanisms, they may decay to the $i$th level by emitting $\gamma$ rays. This is a population fed by the $\gamma$-ray cascade

$\sigma_i^{\rm Cas}$. Here, continuum state refers to the part of the target spectrum which is approximated by a continuous description beyond a given excitation energy for which the individual levels are only partially known, and it is to be distinguished from the quantum mechanics definition of the continuum that lies beyond the particle emission threshold. The $\gamma$-ray production cross section is thus finally given by

$$\sigma(\gamma_{i\to j}) = \left\{\sigma_i^{\rm CN} + \sigma_i^{\rm DI} + \sigma_i^{\rm Cas}\right\} b(i \to j)\frac{1}{1+\alpha}. \quad (4)$$

The direct inelastic scattering process excites low-lying discrete levels. It may excite giant resonances that sit at higher energies as well. The discrete level excitations $\sigma_i^{\rm DI}$ are often calculated by the coupled-channels method where the nuclear states are described by the so-called collective model [53]. For an axially deformed target such as $^{238}$U, a static deformation is usually assumed (rotor model) with possible dynamic oscillations (vibrations in the intrinsic frame). The collective model calculation requires the prior knowledge of spin-parity and excitation energy of the low-lying states, as well as the static and dynamic deformation parameters.

For incident energies up to a few MeV, despite a significant contribution of the direct process, inelastic scattering is dominated by a compound process, namely the formation and decay of a compound nucleus (see Figs. 2 and 3 of Ref. [47]). At higher energies, as the level density increases, the compound process contribution rapidly decreases, and first the direct and then the preequilibrium process dominate.

The compound inelastic scattering is calculated with the statistical Hauser-Feshbach theory with the width fluctuation correction. When the incident neutron energy is not so high, all final states of inelastic scattering are discrete levels and the cross section is written by a compound nucleus formation cross section multiplied by the BR,

$$\sigma_i^{\rm CN} = \sigma^{\rm CN}\frac{T(i \to {\rm CN})}{\sum_j T(j \to {\rm CN})}W_i, \quad (5)$$

where $T(i \to {\rm CN})$ is the neutron transmission coefficient from the $i$th discrete level to the compound state, and $W_i$ is the width fluctuation correction factor. When the incident neutron energy increases, the residual nucleus can also be in a continuum state, and the summation in Eq. (5) is replaced by an appropriate integration over the level density. Obviously $\sigma_i^{\rm CN}$ decreases rapidly, since the denominator of the BR increases with the number of open channels [47]. Note that $W_i$ also depends on the neutron incident channel [54], as well as on the collective excitation [49], which will be discussed later.

Above $\simeq$10 MeV, a nucleon can be scattered to the continuum before the system reaches the equilibrium, and the preequilibrium model describes the inelastic scattering process. This is a part of $\sigma_i^{\rm Cas}$. The pre-equilibrium process proceeds through two distinct mechanisms: the multistep direct mechanism (MSD) where at least one nucleon is in the continuum, or the multistep compound mechanism (MSC) where all the nucleons are bound [55]. Since MSC is a weak process [56], we may omit this from our calculations. A classical approach to the preequilibrium process is given by the exciton model. However, in contrast to the MSC and MSD chains defined by Feshbach's projection operator technique, the exciton model does not respect the configuration space and phenomenologically parametrizes the particle-hole pair creation and annihilation matrix elements. Besides, the exciton model does not conserve the spin and parity. This has a significant impact on $\sigma_i^{\rm Cas}$ as shown by Dashdorj *et al.* [57], and as illustrated later in Sec. IV C.

The calculated level production cross section $\sigma_i$ strongly depends on model input parameters and prescriptions used to describe the various mechanisms at work. For inelastic scattering to the $i$th level, these parameters are

(i) for $\sigma_i^{\rm DI}$, optical potential parameters, the coupling scheme of nuclear states, and nuclear deformation parameters,
(ii) for $\sigma_i^{\rm CN}$, optical potential parameters that provide the transmission coefficients, a method to account for the widths fluctuation correction.

The $\gamma$-ray cascade originates from either a continuum state or a discrete level, and the distinction between the continuum and discrete states are rather arbitrary depending on the selected prescription. Models often rely on a sharp critical energy up to which all the spins and parities of discrete levels are supposed to be known, then they switch to a level density model (see discussion in Sec. V D).

Each of these modeling features has a relative importance that depends on the characteristics of $i$th level and the incident energy considered. This will be discussed in the following sections, where options for modeling of direct excitations, preequilibrium reactions, and the structure of the target nucleus will be compared and their impact on $(n, n'\gamma)$ cross sections will be discussed.

### C. Compound reaction modeling

Inelastic scattering through a compound process [$\sigma_i^{\rm CN}$ in Eq. (5)] is usually modeled following the statistical Hauser-Feshbach theory that replaces the energy-average decay width $\langle\Gamma_c\rangle$ by the optical model transmission coefficients $T_c$. These coefficients are given by solving the single-channel Schrödinger equation for a one-body complex potential. The scattering matrix $S$ is always diagonal, and the transmission coefficient is calculated as $T_c = 1 - |S_{cc}|^2$. However, when excited states are strongly coupled with the ground state, the $S$-matrix of the coupled-channels method is no longer diagonal. In that case, to apply the Hauser-Feshbach model with the width fluctuation correction, we first calculate the Satchler's penetration matrix [58]

$$P_{ab} = \delta_{ab} - \sum_c S_{ac}S_{bc}^*, \quad (6)$$

and diagonalize it by a unitary transformation [59]

$$(UPU^\dagger)_{\alpha\beta} = \delta_{\alpha\beta}p_\alpha, \qquad 0 \leqslant p_\alpha \leqslant 1, \quad (7)$$

where $p_\alpha$ is the transmission coefficient in the diagonal space. The transformation $U$ diagonalizes the matrix $S$ as $\tilde{S} = USU^T$, where the diagonal $\tilde{S}$ includes the single-channel transmission coefficient $p_\alpha$. The statistical model is performed in the diagonal $\tilde{S}$ space to obtain the width fluctuation corrected cross section $\sigma_{\alpha\alpha}$ and $\sigma_{\alpha\beta}$, then the matrix is

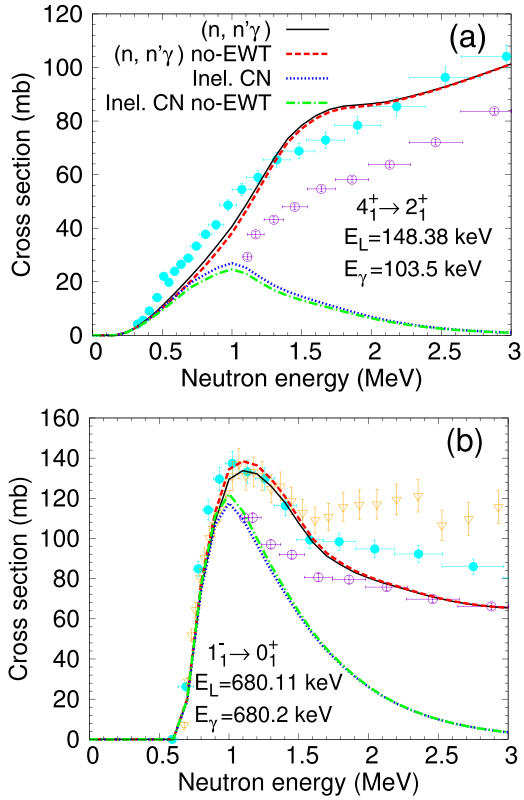


FIG. 9. Calculated $(n, n'\gamma)$ cross sections with (full black curves) and without (dashed red curves) the EWT (see details in Sec. IV C). The contribution from the compound inelastic scattering, that is $\sigma_i^{\rm CN}\frac{b(i\rightarrow j)}{1+\alpha}$, to the $\gamma$-ray production $\sigma(\gamma_{i\rightarrow j})$ [see Eq. (4)] is also displayed as dotted blue curves for calculations with the EWT and dotted-dashed green curves for calculations without. Symbols represent experimental data as defined in Figs. 7 and 8.

transformed back to the cross section space $\sigma_{aa}$ and $\sigma_{ab}$ [60]. This gives a compound nucleus cross section that rigorously accounts for off-diagonal elements in $S$. Because of the unitarity limit constraint, this transformation, often called the Engelbrecht-Weidenmüller transformation (EWT), mitigates the well known enhancement of the elastic channel [50] and enhances the inelastic cross section below 2 MeV as shown in Fig. 9 of [50].

Although this effect should be accounted for in the $n+{}^{238}$U reaction modeling [61,62], its impact on $(n, n'\gamma)$ cross sections remains small in the energy range of our experimental data, as shown in Fig. 9 (top panel) for the $\gamma$ decays of the $4^+_1$ and $1^-_1$ levels, where the $\gamma$-ray productions calculated with (black full curves) and without (red dashed curves) this effect are compared. The population of these levels below 1 MeV is mainly due to the CN inelastic scattering. However, the EWT correction changes the CN cross section by at most 10–20% below 1.5 MeV (compare dotted blue and dot-dashed green curves in Fig. 9). Note that to illustrate how the CN inelastic scattering contributes to the $\gamma$-ray production, the CN inelastic cross sections are weighted by the factor $\frac{b(i\rightarrow j)}{1+\alpha}$ for the transition $i \rightarrow j$ [see Eq. (3)].

## D. Preequilibrium modeling

### 1. Microscopic approaches

In the context of the present work, preequilibrium emission corresponds to the fast emission of a neutron in the continuum, in contrast to inelastic scattering to discrete excitations at low energies. We model the preequilibrium process either with the classical exciton model or with quantum mechanical (QM) microscopic approaches. For the latter, the emission is described as a direct excitation process, and the angular momentum conservation is explicitly included. In the QM approaches, we demonstrate two types of calculations that involve different levels of complexity.

First, we describe the target excited states as one-particle one-hole (1p-1h) excitation of the ground state [57], and one-step DWBA (distorted wave Born approximation) calculations are performed for each of the 1p-1h configurations. As we mainly deal with neutron induced reactions below 20 MeV, contributions by larger number can be neglected.

The second approach is based on the QRPA (quasiparticle random phase approximation) nuclear structure method and approximated projection techniques to define the target excitation in the laboratory frame [63]. First, excitations in the intrinsic frame are defined as one-phonon excitation of the QRPA correlated ground-state. Then we perform a coupled channels calculation which employs couplings between the ground state rotational band and the rotational band states that stem from an intrinsic excitation. Such a coupled channel calculation is repeated for each intrinsic excitation predicted by the QRPA model. A folding model generates the optical potential and form factors that enter the definition of the coupled channels equations. More details of the present JLM/QRPA approach for axial nuclei can be found in Ref. [64]. We add here that HFB (Hartree-Fock-Bogoliubov) and QRPA calculations are performed using a cylindrical harmonic oscillator basis with 13 major shells with the D1S Gogny force [65]. Intrinsic excitations are considered for values of the projection $K$ of the total angular momentum on the nucleus symmetry axis up to 10, and values of the target state spin $J$ and transferred angular momentum $L$ up to 10, for both parities, to ensure a good convergence of our calculations.

### 2. Spin distribution of populated states

The preequilibrium process transfers relatively small angular momentum to the residual nucleus because a limited number of nucleon degrees of freedom are involved. By comparison, in the compound reaction an incident neutron populates a wide range of spin states in the CN, so the neutron emission process enlarges the spin phase space being accessible in the residual nucleus. As shown by Dashdorj *et al.* [57], the spin distribution of populated states by the preequilibrium process modifies the $\gamma$-ray cascade, which results in a significant difference of the discrete $\gamma$-ray production in the $(n, n'\gamma)$ transitions, especially for $\gamma$ decay from high spin levels at incident energies where preequilibrium dominates.

Within a microscopic approach inelastic scatterings to many target states, each of them characterized by an

excitation energy $E_x$, a spin $J$, and a parity $\Pi$, are explicitly calculated, hence the spin-parity distribution of the populated states in the continuum is readily known. The spin distribution of the populated states for the incident neutron energy $E_n$ reads

$$R(J, E_n, E_x) = \sum_{\Pi=\pm 1} \frac{\sigma_{J^\Pi}(E_n, E_x)}{\sum_{J^\Pi} \sigma_{J^\Pi}(E_n, E_x)}, \tag{8}$$

where $\sigma_{J^\Pi}$ is the microscopically calculated inelastic scattering cross section to the $(J, \Pi, E_x)$ state.

The exciton model does not provide the spin-parity distribution of the residual nucleus. TALYS employs an *ad hoc* prescription by Gruppelaar [66] to calculate the spin-parity distribution, which is based on the level density model

$$R_n(J^\Pi) = f_\Pi \frac{2J+1}{\sqrt{\pi} n^3 \sigma_n^3} \exp\left\{-\frac{(J+1/2)^2}{n\sigma_n^2}\right\}, \tag{9}$$

where $n$ is the exciton number and $f_\Pi = \frac{1}{2}$. The spin cutoff parameter is

$$\sigma_n^2 = snA^{2/3}\,. \tag{10}$$

$R_n(J^\Pi)$ satisfies the normalization $\sum_{J^\Pi}(2J+1)R_n(J^\Pi) \simeq 1$ (deviation from unity is less than $10^{-6}$ if $s > 0.006$ for $A = 238$). The $s$-parameter value implemented in the TALYS 1.95 code is $s = 0.24$, following Gruppelaar [66]. The spin-parity distribution of the exciton model is a convolution of the $R_n(J^\Pi)$ distributions with the occupation probabilities for each exciton configuration. If $\sigma_n(E_n, E_x)$ is the pre-equilibrium neutron emission component corresponding to the exciton number $n$, which depends on the incident neutron energy $E_n$ and on the target excitation energy $E_x$, the resulting spin distribution is

$$R(E_n, E_x, J) = \sum_{\Pi=\pm 1} \frac{\sum_n R_n(J^\Pi)\sigma_n(E_n, E_x)}{\sum_n \sigma_n(E_n, E_x)}. \tag{11}$$

Figure 10 compares the spin distribution associated with the exciton model, Eq. (11), to the spin distribution of Eq. (8) calculated from the JLM/QRPA or the DWBA/1p-1h microscopic models. As seen in Figs. 10(b) and 10(c), both microscopic calculations give an average spin in the range $2\hbar$–$6\hbar$ while the minimum value of the exciton model is $9\hbar$ and grows rapidly with the excitation energy as components with higher number of excitons are added. An example of the distribution for the incident (outgoing) energy 10 (5) MeV is shown in Fig. 10(a). While both microscopic models have a very similar width (both centered at $3\hbar$-$4\hbar$) the excitons model is centered at $9\hbar$ and has a very large width.

Consequently, in comparison to the exciton model, the microscopic models strongly suppress the $\gamma$ transitions from levels with spin higher than $6\hbar$, which is demonstrated in Fig. 11 for the $E2$ transitions inside the ground state rotational band: the 159.0-keV ($6^+ \to 4^+$), the 210.6-keV ($8^+ \to 6^+$), and the 257.8-keV ($10^+ \to 8^+$) $\gamma$ rays. Since the preequilibrium process given by microscopic models hardly populates high spin states in the continuum, the experimental data of high-spin transitions, such as $10^+ \to 8^+$, are well reproduced by these models that give a proper ratio of preequilibrium to compound process.

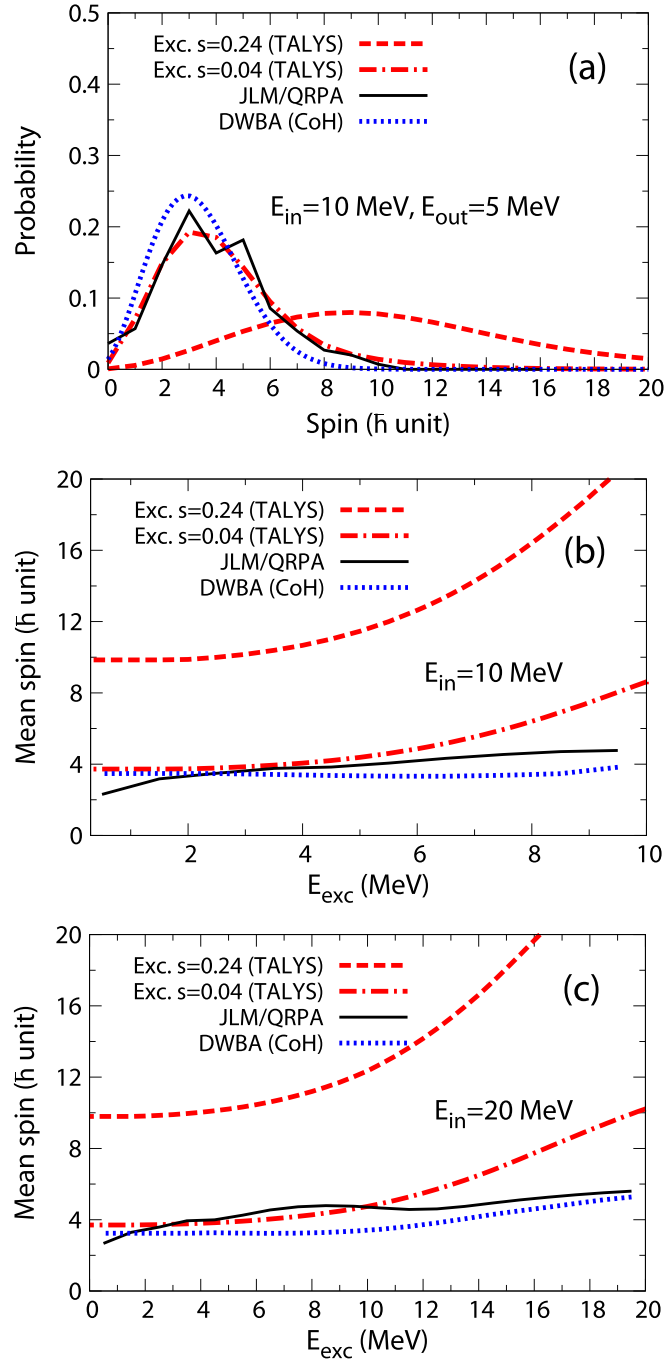


FIG. 10. (a) Spin distribution for the incident energy 10 MeV and an excitation energy of 5 MeV. Average spin as a function of the excitation energy for the two incident energies 10 MeV (b) and 20 MeV (c). On these plots, results from the exciton model are compared to those of the two microscopic preequilibrium models (see Secs. IV D and IV D 2).

Neutron emission for excitation energy above the $^{238}$U neutron separation energy $S_n = 6.154$ MeV does not contribute to $(n, n'\gamma)$ reactions as the excited nucleus will most likely emit a second neutron. Keeping that in mind, we have fitted the cutoff parameter $s$ of Eq. (10) to approximately reproduce the spin distribution of the microscopic models below the

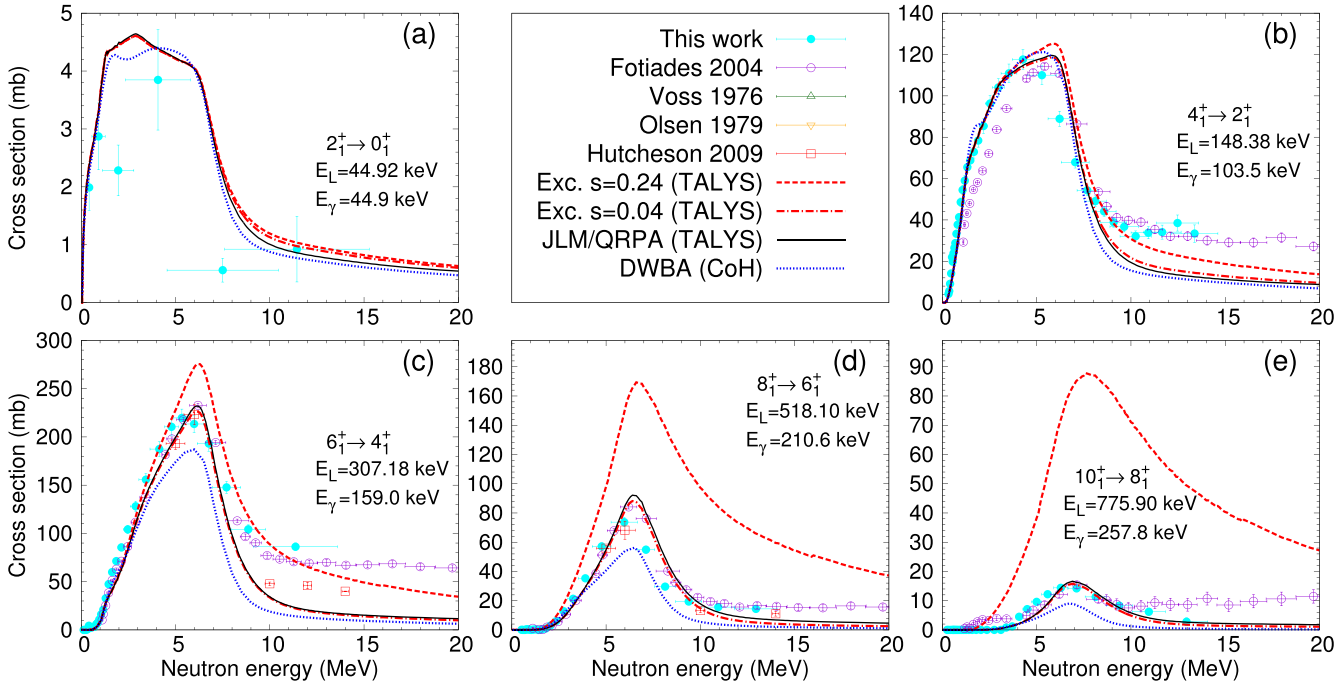


FIG. 11. Data for $^{238}$U$(n, n'\gamma)$ cross sections for transitions within the ground state rotational band. Spin and parity of the initial and final states, energy of the $\gamma$ ray, experimental data (symbols) and calculations (curves) are defined in the plots. Calculations based on four different preequilibrium models are compared: excitons with $s = 0.24$ or $s = 0.04$, JLM/QRPA (TALYS code) and DWBA (CoH code).

excitation energy $E_x = S_n$ (dotted-dashed red curves in Fig. 10) and found the value $s = 0.04$. When the exciton model is used with this value of the spin cutoff parameter, transitions from high spin levels are well reproduced as shown in Fig. 11 (red dotted-dashed curves).

## V. IMPORTANCE OF NUCLEAR STRUCTURE KNOWLEDGE

### A. Experimental $\gamma$ intensity determination

As already mentioned, an important ingredient in the prompt $\gamma$-ray spectroscopy method is the good knowledge of the nuclei structure information. With our measurements, when we are able to measure the deexcitation of a level by several $\gamma$ rays, we can deduce the $\gamma$ intensity and check the value in the ENSDF database [38] or in other nuclear structure experiments such as those by Govor *et al.* [67]. Most of the BRs in ENSDF come from Coulex experiments and particularly from McGowan *et al.* [68]. The data from Govor *et al.* have been obtained in a $(n, n'\gamma)$ experiment after an irradiation of $^{238}$U with a beam of reactor fast neutrons. We have calculated $\gamma$ intensity for all levels where it was possible and the results are summarized in Table IV. This study reveals discrepancies between our and previous works for levels at 680.11, 950.12, and 997.58 keV. For the last one, discrepancy stays nevertheless within the uncertainty with regards to ENSDF. Figure 12 illustrates the calculated ratio of $\gamma$ intensity for the levels at 680.11 and 997.58 keV. We note that, as this ratio has to be constant, it was calculated for the neutron energy range where it is effectively constant. Indeed, for low neutron energies we are sensitive to threshold effect and, at high neutron energy where the $(n, n'\gamma)$ cross sections are very low, we are sensitive to statistics variations but also to possible contaminations by $(n, 2n)$ processes. For the level at 680.11 keV, our result coincides with Govor *et al.* but is in disagreement with ENSDF. Considering the level at 950.12 keV, our measurement is in disagreement with ENSDF, especially for the 270.1-keV $\gamma$ ray. The values from Govor *et al.* show that the intensities of the 270.1- and 218.1-keV transitions are inverted compared to ENSDF and our values. If this inversion is due to a typo in the article, then our values would be in good

TABLE IV. $\gamma$ intensities calculated in this work compared to ENSDF and Govor *et al.* [67] values.

| $E_{\text{level}}$ (keV) | $E_\gamma$ (keV) | $I_\gamma$ this work | $I_\gamma$ ENSDF | $I_\gamma$ Govor *et al.* |
|---|---|---|---|---|
| 680.11 | 680.2 | 61 (7) | 79 (4) | 61 |
| | 635.3 | 100 | 100 (2) | 100 |
| 731.93 | 583.55 | 84 (3) | 81.4 (16) | 85 |
| | 686.99 | 100 | 100 (2) | 100 |
| 826.64 | 519.46 | 55 (2) | 50 (3) | 56 |
| | 678.3 | 100 | 100 (6) | 100 |
| 930.55 | 251.2 | 11 (2) | 13.1 (4) | 8.7 |
| | 885.46 | 100 | 100 (4) | 100 |
| 950.12 | 270.1 | 28 (3) | 48 (8) | 37 |
| | 218.1 | 41 (8) | 53 (6) | 27 |
| | 905.5 | 100 | 100 (6) | 100 |
| 997.58 | 952.65 | 64 (9) | 56.8 (13) | 55 |
| | 849.1 | 100 | 100 (3) | 100 |

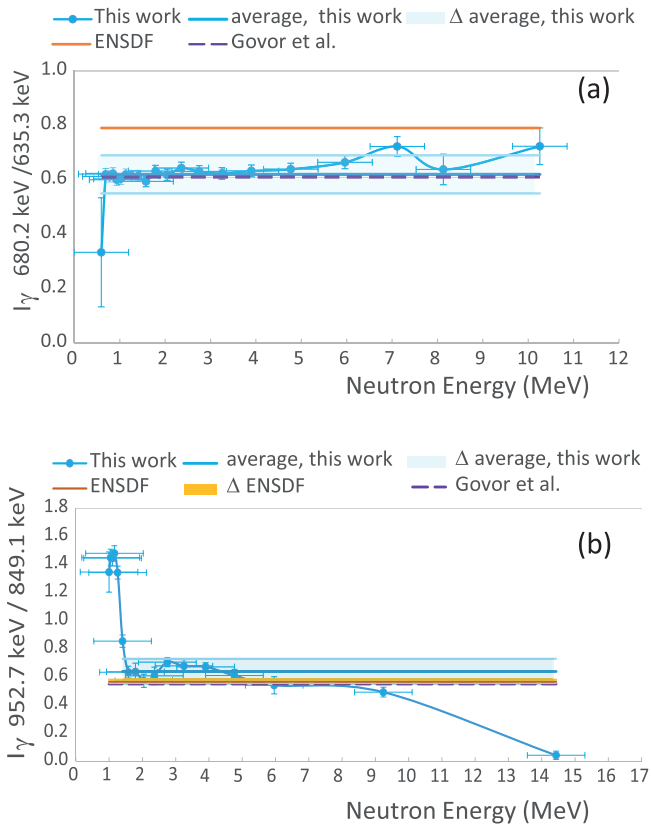


FIG. 12. Ratio of $\gamma$ intensity obtained for the levels at 680.11 keV (a) and 997.58 keV (b), compared to values from ENSDF and from reference Govor *et al.* [67].

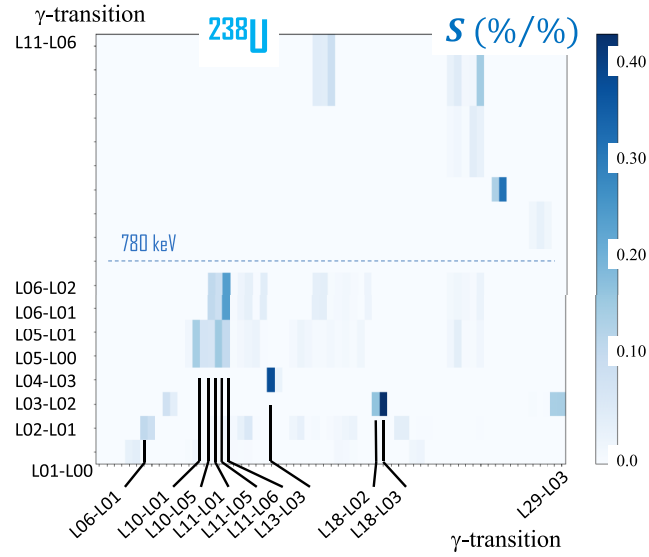


FIG. 13. Sensitivity matrix for calculated $\gamma$-production cross sections for 1.2 MeV incident neutron energy to BRs in $^{238}$U. $L_i$ is the number of the level in TALYS (figure from Ref. [20]).

agreement. We could also point out that from the level at 930.55 keV, another $\gamma$ (931.1 keV) is present in the ENSDF data file with a relative intensity of 25.2 (13). This intensity is stronger than the one of the 251.2-keV $\gamma$ ray that we measured. From the value of the cross section measured for the 885.5-keV $\gamma$ ray, one can deduce a maximum of the cross section at $\simeq 45$ mb for the 931.1 keV $\gamma$-ray that should be observed with GRAPhEME. Nevertheless, as shown in the Fig. 3, only a very small peak is present in the $\gamma$-ray energy distribution at 931 keV. In the results of Govor *et al.*, this $\gamma$ transition is associated with a relative intensity of 5.2, corresponding to a maximum of the cross section amplitude around 9 mb, which is near the limit of detection of GRAPhEME in this experiment. This could suggest a wrong intensity referenced in ENSDF for the 931.1-keV $\gamma$ ray.

Moreover, in $^{238}$U and up to $E_i = 1.3$ MeV (which is the energy of the highest level for which we have been able to detect the $\gamma$ decay), 79 $\gamma$ transitions are listed in ENSDF; 76% have BR information and only 56% are mentioned with uncertainty. The impact of this lack of knowledge on the discrete nuclear structure should be quantified to estimate the error induced in the $(n, n')$ cross section calculation from $(n, n'\gamma)$ measurements.

### B. Sensitivity study with MC calculations

We developed a Monte Carlo simulation based on the TALYS 1.8 code which allows us to estimate the sensitivity of a calculated $\gamma$-transition cross section to the uncertainty on BRs of other $\gamma$ transitions. One by one, the $\gamma$-ray BRs are varied following a Gaussian distribution of standard deviation 10% around the reference value (concurrent transitions are renormalized accordingly). For each realization of a BR value, TALYS is run and calculates the cross sections for all $\gamma$ rays in the nucleus. This is done 100 times per transition and all the outputs are collected and processed with the *cov* function of the Python numpy package [69,70] to produce a correlation matrix (in Fig. 13) that shows the amount of variation of the $\gamma$-ray production cross section for 1.2 MeV incident neutron energy around its central value, for a given relative variation around a specific BR (more information on the method is given in [19]).

One sees that, for transitions decaying from levels 6 ($3^-_1$), 5 ($1^-_1$), 4 ($6^+_1$), and 3 ($4^+_1$), the calculated $\gamma$-production cross sections are sensitive to the BRs and an uncertainty on BR of 10% can lead to an uncertainty on cross section values of around 4%. The changes in BR values that have a major impact on other transitions are emphasized in Fig. 13 (transition in bold on the x-axis). For instance, a change of 10% in the BR value for the L18-L03 transition leads to a change of about 4% of the $\gamma$ production for the L03-L02 transition. In ENSDF, the average BR uncertainty is 8%, thus this information plays a significant role in the uncertainty estimation when inferring the $(n, n')$ cross sections from $(n, n'\gamma)$ ones.

### C. Discrete structure and interband transition

The specific shape of a $\gamma$-ray production for an inter-band transition (see Figs. 7 and 8) can be related to the fact that the decaying level is strongly produced by the decay of a

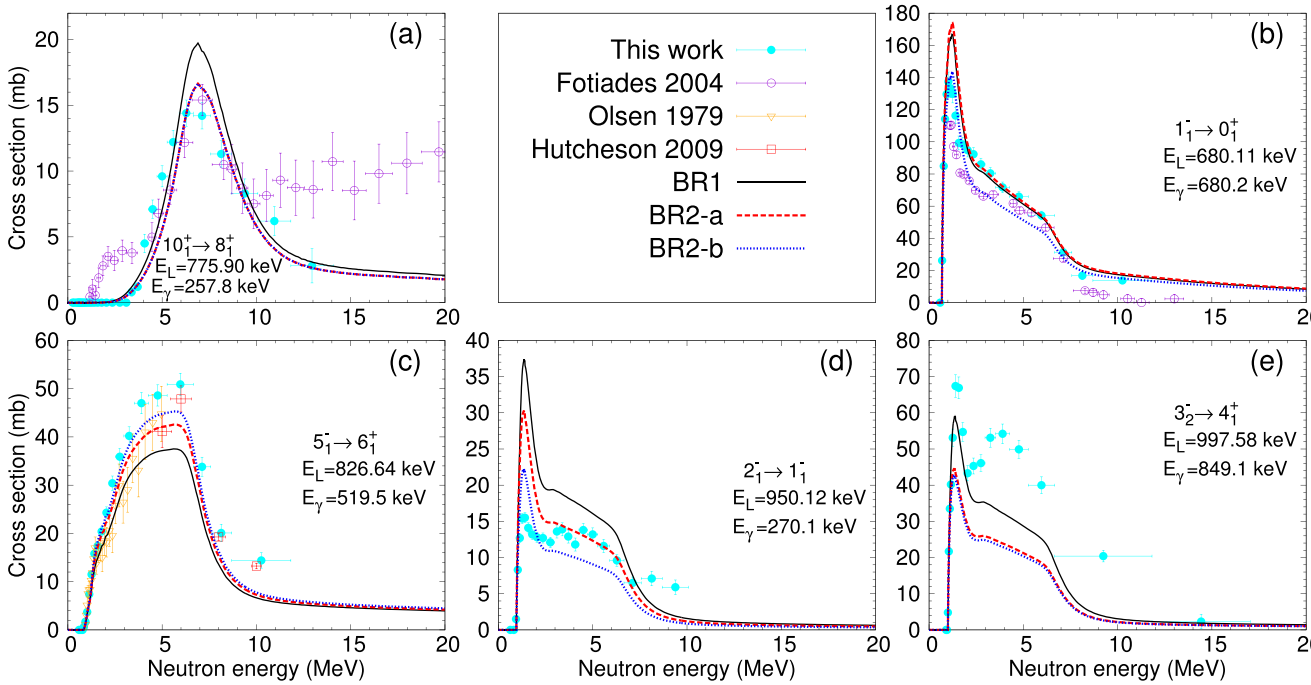


FIG. 14. Experimental $^{238}$U$(n, n'\gamma)$ cross sections (symbols) compared to the nuclear reaction code calculations with various BR determination methods (see Sec. V C).

few discrete levels at higher excitation energy. Consequently, modeling these transitions requires a very good knowledge of the decay scheme and more precisely of the BRs. Discrepancy between theory and measurements can reveal that BRs are not adequate (in terms of their overall magnitude) or that the production by one or several parent levels is not well accounted for. Note that all the interband transitions reported here decay from levels with spin $J \leqslant 5$, so they are almost not impacted by the variations of spin distributions of the residual nucleus that occurs when the preequilibrium model is changed.

BR values reported in the RIPL3 [71] nuclear structure database are used in all calculations reported above. We investigated some assumptions for unknown $\gamma$-ray BRs (indicated as zero in RIPL3). We consider the next three prescriptions:

(i) BR1: if $E1$ transitions are possible, we assume an equal branching for each of them and no other transition. If no $E1$ transition is possible, we assume an equal branching to all daughter levels (prescription used in model B performed with CoH).

(ii) BR2-a: uses a single particle estimate of Weisskopf (see Eqs. (6.8) and (6.9) of [72]). In this case, transition rates to all daughter levels are calculated for all the possible EL and ML transitions (only transitions with a corresponding BR value above 0.1% are kept).

(iii) BR2-b: uses the same approximation as BR2-a and the BR values corresponding to the $\gamma$ intensities given in the third column of Table IV.

We note that the database we used in the TALYS 1.95 calculations displayed in Figs. 7, 8, and 11 was also generated from the RIPL3 database and the BR1 prescription to mimic the discrete decay scheme used in both CoH and EMPIRE calculations. Figure 14 displays the comparison between TALYS calculations performed with BR1, BR2-a, and BR2-b decay schemes and measurements for a few transitions. Using either of the two prescriptions BR1 or BR2-a may improve or deteriorate the calculated transitions. This unclear picture pinpoints that a more thorough study of the unknown transitions in RIPL is needed to improve the modeling at this point. However, using the $\gamma$ intensities deduced from the present measurements (BR2-b) improves the overall agreement between calculations and data. For the $1^-_1$-$0^+_1$ transition, the improvement has two origins: first, the $\gamma$ intensity for the 680.2-keV transition is reduced; second, the $1^-_1$ level production is reduced as well, since the intensities of the 270.1- and 251.2-keV $\gamma$ rays, that populate to the $1^-_1$ level, are also reduced. By reducing the uncertainties on the nuclear structure information, the present measurements offer a way to better understand other modeling aspect.

### D. Discrete levels embedded in the continuum

The level descriptions used in the modeling usually switches from a discrete structure (discrete energies and BRs) to a continuum structure (level densities and $\gamma$-strength functions) at the excitation energy where individual levels are thought to be missing. For $^{238}$U, the level scheme is assumed to be complete up to 40 excited levels, the last level lying at 1.318 MeV [71]. It is, however, possible to use the experimen-

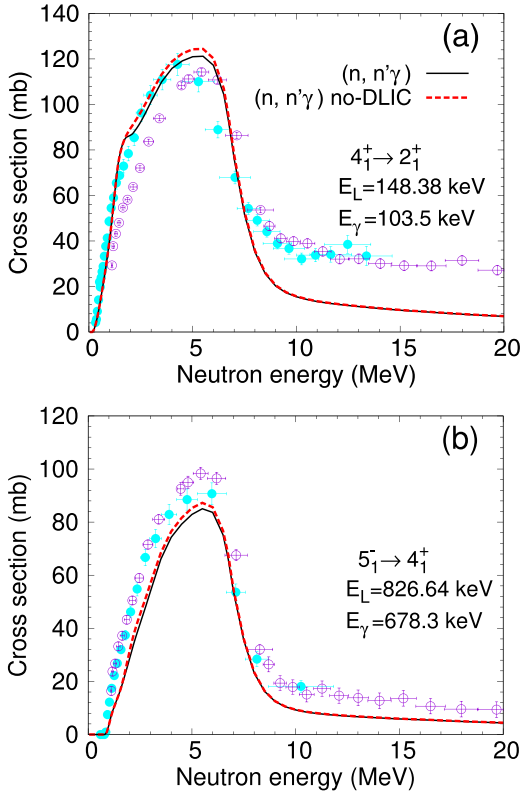


FIG. 15. $(n, n'\gamma)$ cross sections calculated with (full black curves) and without (dashed red curves) discrete states embedded in the continuum (see Sec. V D). Symbols represent experimental data as defined in Figs. 7 and 8.

tally known discrete levels above this energy by combining a discrete and continuum description, i.e., embedding discrete levels in the continuum. This was shown to be important in reproducing $^{182,184,186}$W$(n, n'\gamma)$ cross section data [20,73].

We applied this method to the present $^{238}$U$(n, n'\gamma)$ reaction modeling with the CoH code. Embedding 54 discrete levels in the continuum increases the $\gamma$ production by a few percent for intraband transitions, as illustrated in Fig. 15 for the $6^+_1$-$4^+_1$ transition. Impact on the interband transitions is negligible (not shown). This information is important to achieve a good understanding of $(n, n'\gamma)$ modeling and to avoid compensation effects between the various modeling aspects.

## VI. CONCLUSIONS

The prompt $\gamma$-ray spectroscopy method used with the GRAPhEME setup is a powerful method to produce precise $(n, xn\gamma)$ cross section data valuable for studying reaction models and improving the quality of evaluated nuclear data files. We have shown that the $(n, n'\gamma)$ cross sections can be used as a fine probe to pinpoint shortcomings in both reaction modeling and nuclear structure knowledge.

Microscopic modeling of the preequilibrium emission improves the description of the $(n, n'\gamma)$ reactions as it predicts spin distributions of the residual nucleus that account for the cross section contributions caused by $\gamma$ decay from high spin levels (decay of $8^+$ and $10^+$ levels). While it improves the description on compound inelastic scattering, the inclusion of the Engelbrecht-Weidenmüller transformation in the width fluctuation correction did not impact significantly the calculation of the $(n, n'\gamma)$ cross sections in the energy range of our experimental data. Some of the interband transitions are shown to be very sensitive to the choice of prescription for discrete levels $\gamma$ decay that are not given in the RIPL3 library.

New branching ratios were extracted from the present measurements, which, when used in the modeling, seem to improve the theory/experiment agreement. Discrete states in the continuum are shown to play a role in the data/modeling agreement. This reveals the importance of $(n, xn\gamma)$ studies of recent refinements implemented in nuclear reaction codes, but also reveals defects that need further consideration.

Large uncertainties in the current modeling are related to the knowledge of the decay scheme: poorly known branching ratios and an incomplete information of the discrete states above 1.3 MeV. With a Monte Carlo type approach, we showed that 10% of uncertainty on the BR values leads to an uncertainty on the calculated cross sections of around 4%. That effect should be considered if total $(n, n')$ cross sections are inferred from partial $(n, n'\gamma)$ cross section data.

Involving nuclear structure theory, such as the QRPA approach, could be helpful in providing new constraints or guidance to complete the structure knowledge. A deeper review of the $\gamma$-decay scheme from the RIPL3 library could be of interest as well. Other aspects of the modeling, such as variation of the $E1$ and $M1$ strength functions that define the $\gamma$ decay from continuum levels, were shown to be of importance [20] and should be studied more in detail in the context of $(n, n'\gamma)$ reactions.

As mentioned in the Introduction, in a next step, all the cross sections obtained in the frame of this new measurement on $^{238}$U and the improvements performed on modeling will be used to produce total neutron inelastic scattering cross section of $^{238}$U. We also mention that the results reported here are part of a more comprehensive experimental work performed with GRAPhEME which will lead to new $(n, xn\gamma)$ cross section data on $^{238}$U, $^{182,184,186}$W, and $^{232}$Th (publications in preparation).

## ACKNOWLEDGMENTS

The authors thank the team of the GELINA facility for the preparation of the neutron beam and for their strong support day after day. This work was partly supported by PACEN/GEDEPEON, then NEEDS, and by the European Commission within the Sixth Framework Programme through I3-EFNUDAT (EURATOM Contract No. 036434) and NUDAME (Contract No. FP6-516487), and within the Seventh Framework Programme through EUFRAT (EURATOM Contract No. FP7-211499), through ANDES (EURATOM Contract No. FP7-249671), and through CHANDA (EURATOM Contract No. FP7-605203). This project has received funding from the Euratom Research and Training Programme 2014-2018 under Grant Agreement No. 847552.

[1] M. Salvatores and R. Jacqmin, OECD-NEA Technical Report No. 6410, 2008 (unpublished).

[2] A. Santamarina, D. Bernard, P. Leconte, and J.-F. Vidal, Nucl. Data Sheet **118**, 118 (2014).

[3] A. Santamarina, D. Bernard, P. Blaise, M. Coste, A. Courcelle, T. Huynh, C. Jouanne, P. Leconte, O. Litaize, S. Mengelle *et al.*, OECD-NEA Technical Report No. 6190, 2006 (unpublished).

[4] OECD-NEA, Nuclear data high priority request list, online: http://www.nea.fr/dbdata/hprl/.

[5] N. Otuka, E. Dupont, V. Semkova, B. Pritychenko, A. Blokhin, M. Aikawa, S. Babykina, M. Bossant, G. Chen, S. Dunaeva *et al.*, Nucl. Data Sheets **120**, 272 (2014).

[6] N. Fotiades, G. D. Johns, R. O. Nelson, M. B. Chadwick, M. Devlin, W. S. Wilburn, P. G. Young, J. A. Becker, D. E. Archer, L. A. Bernstein, P. E. Garrett, C. A. McGrath, D. P. McNabb, and W. Younes, Phys. Rev. C **69**, 024601 (2004).

[7] N. V. Kornilov and A. B. Kagalenko, Nucl. Sci. Eng. **120**, 55 (1995).

[8] R. R. Winters, N. W. Hill, R. L. Macklin, J. A. Harvey, D. K. Olsen, and G. L. Morgan, Nucl. Sci. Eng. **78**, 147 (1981).

[9] V. Andreev, Neitronnaya Fizika, Moskva 287 (1961) [Sov. Prog. Neutron Phys. 211 (1963)].

[10] L. L. Litvinsky, A. V. Murzin, G. M. Novoselov, and O. A. Purtov, Yad. Fiz. **52**, 1025 (1990) [Sov. J. Nucl. Phys. **52**, 652 (1990)].

[11] L. Cranberg and J. Levin, Phys. Rev. **109**, 2063 (1958).

[12] M. C. Moxon, J. A. Wartena, H. Weigmann, and G. J. Vanpraet, in *Proceedings of the International Confrence on Nuclear Data for Science and Technology, Gatlinburg* (American Nuclear Society, 1994).

[13] M. Baba, H. Wakabayashi, N. Ito, K. Maeda, and N. Hirakawa, J. Nucl. Sci. Technol. **27**, 601 (1990).

[14] N. Glazkov, Atom. Energ. **14**, 400 (1963) [Sov. Atom. Energy **14**, 405 (1964)].

[15] F. Tsang and R. Brugger, Nucl. Sci. Eng. **65**, 70 (1978).

[16] A. B. Smith and P. T. Guenther, ANL/NDM Technical Report No. 63, 1982 (unpublished).

[17] A. Smith and P. Guenther, *Nuclear Data for Science and Technology: Proceedings of the International Conference Antwerp, 1982*, edited by K. H. Bockhoff (Springer, Netherlands, 1983).

[18] M. Chadwick, E. Dupont, E. Bauge, A. Blokhin, O. Bouland, D. Brown, R. Capote, A. Carlson, Y. Danon, C. D. S. Jean *et al.*, Nucl. Data Sheets **118**, 1 (2014).

[19] M. Kerveno, G. Henning, C. Borcea, P. Dessagne, M. Dupuis, S. Hilaire, A. Negret, M. Nyman, A. Olacel, E. Party *et al.*, EPJ Nucl. Sci. Technol. **4**, 23 (2018).

[20] M. Kerveno, M. Dupuis, C. Borcea, M. Boromiza, R. Capote, P. Dessagne, G. Henning, S. Hilaire, T. Kawano, A. Negret *et al.*, EPJ Web Conf. **239**, 01023 (2020).

[21] K. Shibata, O. Iwamoto, T. Nakagawa, N. Iwamoto, A. Ichihara, S. Kunieda, S. Chiba, K. Furutaka, N. Otuka, T. Ohsawa *et al.*, J. Nucl. Sci. Technol. **48**, 1 (2011).

[22] A. Plompen, O. Cabellos, C. De Saint Jean *et al.*, Eur. Phys. J. A **56**, 181 (2020).

[23] M. Chadwick, M. Herman, P. Obložinský, M. Dunn, Y. Danon, A. Kahler, D. Smith, B. Pritychenko, G. Arbanas, R. Arcilla *et al.*, Nucl. Data Sheets **112**, 2887 (2011).

[24] D. Brown, M. Chadwick, R. Capote, A. Kahler, A. Trkov, M. Herman, A. Sonzogni, Y. Danon, A. Carlson, M. Dunn *et al.*, Nucl. Data Sheets **148**, 1 (2018), Special Issue on Nuclear Reaction Data.

[25] G. Zhigang, X. Ruirui, W. Haicheng, Z. Yue, C. Guochang, J. Yongli, S. Nengchuan, C. Yongjing, T. Xi, T. Yuan *et al.*, EPJ Web Conf. **239**, 09001 (2020).

[26] ROSFOND-2010: Updated Russian Library of Evaluated Neutron Data, online: http://www-nds.iaea.org/exfor/endf.htm.

[27] M. Kerveno, J. C. Thiry, A. Bacquias, C. Borcea, P. Dessagne, J. C. Drohé, S. Goriely, S. Hilaire, E. Jericha, H. Karam, A. Negret, A. Pavlik, A. J. M. Plompen, P. Romain, C. Rouki, G. Rudolf, and M. Stanoiu, Phys. Rev. C **87**, 024609 (2013).

[28] M. Kerveno, A. Bacquias, C. Borcea, P. Dessagne, G. Henning, A. Negret, M. Nyman, A. Olacel, A. Plompen, C. Rouki *et al.*, Eur. Phys. J. A **51**, 167 (2015).

[29] D. Tronc, J. Salomé, and K. Böckhoff, Nucl. Instrum. Methods Phys. Res. A **228**, 217 (1985).

[30] D. Ene, C. Borcea, S. Kopecky, W. Mondelaers, A. Negret, and A. Plompen, Nucl. Instrum. Methods Phys. Res. A **618**, 54 (2010).

[31] M. Flaska, A. Borella, D. Lathouwers, L. Mihailescu, W. Mondelaers, A. Plompen, H. van Dam, and T. van der Hagen, Nucl. Instrum. Methods Phys. Res. A **531**, 392 (2004).

[32] L. Arnold, R. Baumann, E. Chambit, M. Filliger, C. Fuchs, C. Kieber, D. Klein, P. Medina, C. Parisel, M. Richer *et al.*, in *14th IEEE-NPSS Real Time Conference, 2005* (IEEE, Piscataway, NJ, 2005), pp. 265–269.

[33] MCNPX, online: http://mcnpx.lanl.gov/.

[34] LENNTECH, online: https://www.lenntech.fr/francais/data-perio/u.htm.

[35] D. C. Radford, gf3, online: http://radware.phy.ornl.gov/gf3/gf3.html.

[36] A. Carlson, V. Pronyaev, R. Capote, T. Kawano, H. Hofmann, H. Vonach, and S. Tagesen, Nucl. Data Sheets **148**, 143 (2018).

[37] C. R. Brune, Nucl. Instrum. Methods Phys. Res. A **493**, 106 (2002).

[38] E. Browne and J. Tuli, Nucl. Data Sheets **127**, 191 (2015).

[39] F. Voss, S. Cierjacks, D. Erbe, and G. Schmatz, Kernforschungszentrum Karlsruhe Report No. 2379, 1976 (unpublished).

[40] D. Olsen, G. Morgan, and J. McConnell, in *Proceedings of the International Conference on Nuclear Cross Sections for Technology*, Knoxville, TN, 22–26 October 1979, edited by J. L. Fowler, C. H. Johnson, and C. D. Bowman (National Bureau of Standards, Washington, 1979), p. 677.

[41] A. Hutcheson, C. Angell, J. A. Becker, A. S. Crowell, D. Dashdorj, B. Fallin, N. Fotiades, C. R. Howell, H. J. Karwowski, T. Kawano, J. H. Kelley, E. Kwan, R. A. Macri, R. O. Nelson, R. S. Pedroni, A. P. Tonchev, and W. Tornow, Phys. Rev. C **80**, 014603 (2009).

[42] T. Kibédi, T. Burrows, M. Trzhaskovskaya, P. Davidson, and J. C. W. Nestor, Nucl. Instrum. Methods A **589**, 202 (2008).

[43] A. Olacel, C. Borcea, M. Boromiza, P. Dessagne, G. Henning, M. Kerveno, A. Negret, M. Nyman, and A. Plompen, EPJ Web Conf. **239**, 01040 (2020).

[44] L. Mihailescu, C. Borcea, A. Koning, and A. Plompen, Nucl. Phys. A **786**, 1 (2007).

[45] F. Voss, S. Cierjacks, D. Erbe, and G. Scmalz, in *Nuclear Cross Sections and Technology: Proceedings of a Conference,*

*Washington, , 1975*, edited by R. A. Schrack and C. D. Bowman (National Bureau of Standards, Washington, 1975), p. 916.
[46] F. Chukreev, V. Makarenko, and M. Martin, Nucl. Data Sheets **97**, 129 (2002).
[47] P. Romain, B. Morillon, and H. Duarte, Nucl. Data Sheets **131**, 222 (2016), Special Issue on Nuclear Reaction Data.
[48] T. Kawano, in *Compound-Nuclear Reactions*, edited by J. Escher, Y. Alhassid, L. A. Bernstein, D. Brown, C. Fröhlich, P. Talou, and W. Younes (Springer International, Cham, 2021), pp. 27–34.
[49] T. Kawano, R. Capote, S. Hilaire, and P. Chau Huu-Tai, Phys. Rev. C **94**, 014612 (2016).
[50] T. Kawano, Eur. Phys. J. A **57**, 16 (2021).
[51] R. Capote, A. Trkov, M. Sin, M. T. Pigni, V. G. Pronyaev, J. Balibrea, D. Bernard, D. Cano-Ott, Y. Danon, A. Daskalakis *et al.*, Nucl. Data Sheets **148**, 143 (2018).
[52] M. Herman, R. Capote, M. Sin, A. Trkov, B. Carlson, P. Oblozinsky, M. C. M., H. Wienkey, S. Hoblit, Young-Sik Cho *et al.*, Brookhaven National Laboratory Technical Report No. INDC(NDS)-0603, BNL-101378-2013, 2013 (unpublished).
[53] T. Tamura, Annu. Rev. Nucl. Sci. **19**, 99 (1969).
[54] T. Kawano, P. Talou, and H. A. Weidenmüller, Phys. Rev. C **92**, 044617 (2015).
[55] H. Feshbach, A. Kerman, and S. Koonin, Ann. Phys. (NY) **125**, 429 (1980).
[56] T. Kawano, Phys. Rev. C **59**, 865 (1999).
[57] D. Dashdorj, T. Kawano, P. E. Garrett, J. A. Becker, U. Agvaanluvsan, L. A. Bernstein, M. B. Chadwick, M. Devlin, N. Fotiades, G. E. Mitchell, R. O. Nelson, and W. Younes, Phys. Rev. C **75**, 054612 (2007).
[58] G. R. Satchler, Phys. Lett. **7**, 55 (1963).
[59] C. A. Engelbrecht and H. A. Weidenmüller, Phys. Rev. C **8**, 859 (1973).
[60] H. M. Hofmann, J. Richert, J. W. Tepel, and H. A. Weidenmüller, Ann. Phys. (NY) **90**, 403 (1975).
[61] R. Capote, A. Trkov, M. Sin, M. Herman, and Soukhovitskiĭ, EPJ Web Conf. **69**, 00008 (2014).
[62] R. Capote, A. Trkov, M. Sin, M. Herman, A. Daskalakis, and Y. Danon, Nucl. Data Sheets **118**, 26 (2014).
[63] P. Ring and P. Schuck, *The Nuclear Many-Body Problem* (Springer-Verlag, Berlin, 1980).
[64] M. Dupuis, S. Hilaire, S. Péru, E. Bauge, M. Kerveno, P. Dessagne, and G. Henning, EPJ Web Conf. **146**, 12002 (2017).
[65] S. Péru, G. Gosselin, M. Martini, M. Dupuis, S. Hilaire, and J. C. Devaux, Phys. Rev. C **83**, 014314 (2011).
[66] H. Gruppelaar, Brookhaven National Laboratory Technical Report, 1983 (unpublished).
[67] L. Govor, A. Demidov, V. Kurkin, and I. Mikhailov, Phys. At. Nucl. **77**, 131 (2014).
[68] F. McGowan and W. Milner, Nucl. Phys. A **571**, 569 (1994).
[69] T. E. Oliphant, *A Guide to NumPy*, Vol. 1 (Trelgol, USA, 2006).
[70] S. Van Der Walt, S. C. Colbert, and G. Varoquaux, Comput. Sci. Eng. **13**, 22 (2011).
[71] R. Capote, M. Herman, P. Obložinský, P. Young, S. Goriely, T. Belgya, A. Ignatyuk, A. Koning, S. Hilaire, V. Plujko *et al.*, Nucl. Data Sheets **110**, 3107 (2009), Special Issue on Nuclear Reaction Data.
[72] *Theoretical Nuclear Physics*, edited by J. M. Blatt and V. F. Weisskopf (Springer-Verlag, New York, 1979).
[73] G. Henning, A. Bacquias, C. Borcea, M. Boromiza, R. Capote, P. Dessagne, J.-C. Drohé, M. Dupuis, S. Hilaire, T. Kawano *et al.*, in PHYSOR 2020: Transition to a Scalable Nuclear Future, UK, 2020 (unpublished), https://hal.archives-ouvertes.fr/hal-02956052.